Since January 2020 Elsevier has created a COVID-19 resource centre with free information in English and Mandarin on the novel coronavirus COVID-19. The COVID-19 resource centre is hosted on Elsevier Connect, the company's public news and information website.

Journal of Ethnopharmacology 291 (2022) 115038

Contents lists available at ScienceDirect

Journal of Ethnopharmacology

journal homepage: www.elsevier.com/locate/jethpharm

Chemical profiling and unraveling of anti-COVID-19 biomarkers of red sage (*Lantana camara* L.) cultivars using UPLC-MS/MS coupled to chemometric analysis, *in vitro* study and molecular docking

Reham S. Darwish [a], Alaa A. El-Banna [a], Doaa A. Ghareeb [b,c], Mostafa F. El-Hosseny [d], Mohamed G. Seadawy [d], Hend M. Dawood [a,*]

[a] *Department of Pharmacognosy, Faculty of Pharmacy, Alexandria University, Alexandria, Egypt*
[b] *Biological Screening and Preclinical Trial Laboratory, Department of Biochemistry, Faculty of Science, Alexandria University, Alexandria, Egypt*
[c] *Pharmaceutical and Fermentation Industries Development Centre, City of Scientific Research and Technological Applications (SRTA-City), Borg Al-Arab, Alexandria, Egypt*
[d] *Biological Prevention Department, Egyptian Army, Egypt*

ARTICLE INFO

Keywords:
Lantana camara L. cultivars
UPLC-MS/MS
Multivariate analysis
anti-COVID-19 activity
Biomarkers
Molecular docking

ABSTRACT

Ethnopharmacological relevance: Red sage (*Lantana camara* L.) (Verbenaceae) is a widely spread plant that was traditionally used in Brazil, India, Kenya, Thailand, Mexico, Nigeria, Australia and Southeast Asia for treating several ailments including rheumatism and leprosy. Despite its historical role in relieving respiratory diseases, limited studies progressed to the plant's probable inhibition to respiratory viruses especially after the striking spread of severe acute respiratory syndrome coronavirus 2 (SARS-CoV-2) infections.

Aim of the study: This study aimed to investigate the inhibitory activity of different *L. camara* cultivars to SARS-CoV-2, that was not previously inspected, and clarify their mechanisms of action in the metabolomics viewpoint, and to determine the biomarkers that are related to such activity using UPLC-MS/MS coupled to *in vitro*-studies and chemometric analysis.

Materials and methods: Chemical profiling of different cultivars was accomplished via UPLC-MS/MS. Principle component analysis (PCA) and orthogonal projection to latent structures (OPLS) models were built using SIMCA® (multivariate data analysis software). Cytotoxicity and COVID-19 inhibitory activity testing were done followed by TaqMan Real-time RT-PCR (Reverse transcription polymerase chain reaction) assay that aimed to study extracts' effects on RNA-dependent RNA polymerase (RdRp) and E-genes expression levels. Detected biomarkers from OPLS analysis were docked into potential targets pockets to investigate their possible interaction patterns using Schrodinger® suite.

Results: UPLC-MS/MS analysis of different cultivars yielded 47 metabolites, most of them are triterpenoids and flavonoids. PCA plots revealed that inter-cultivar factor has no pronounced effect on the chemical profiles of extracts except for *L. camara*, cultivar Drap d'or flowers and leaves extracts as well as for *L. camara* cv Chelsea gem leaves extract. Among the tested extracts, flowers and leaves extracts of *L. camara* cv Chelsea gem, flowers extracts of *L. camara* cv Spreading sunset and *L. camara* cv Drap d'or showed the highest selectivity indices scoring 12.3, 10.1, 8.6 and 7.8, respectively, indicating their relative high safety and efficacy. Leaves and flowers extracts of *L. camara* cv Chelsea gem, flowers extracts of *L. camara* cv Spreading sunset and *L. camara* cv Drap d'or were the most promising inhibitors to viral plaques exhibiting IC_{50} values of 3.18, 3.67, 4.18 and 5.01 μg/mL, respectively. This was incremented by OPLS analysis that related their promising COVID-19 inhibitory activities to the presence of twelve biomarkers. Inhibiting the expression of RdRp gene is the major mechanism behind the antiviral activity of most extracts at almost all concentration levels. Molecular docking of the active biomarkers against RdRp revealed that isoverbascoside, luteolin-7,4'-O-diglucoside, camarolic acid and lantoic acid exhibited higher docking scores of −11.378, −10.64, −6.72 and −6.07 kcal/mol, respectively, when compared to remdesivir (−5.75 kcal/mol), thus these four compounds can serve as promising anti-COVID-19 candidates.

* Corresponding author.Alkhartoom Square, Department of Pharmacognosy, Faculty of Pharmacy, Alexandria University, Alexandria, 21521, Egypt.
E-mail address: henddawoodpharm@hotmail.com (H.M. Dawood).

https://doi.org/10.1016/j.jep.2022.115038
Received 27 November 2021; Received in revised form 13 January 2022; Accepted 23 January 2022
Available online 10 February 2022

Conclusion: Flowers and leaves extracts of four *L. camara* cultivars were recognized as rich sources of phytoconstituents possessing anti-COVID-19 activity. Combination of UPLC-MS/MS and chemometrics is a promising approach to detect chemical composition differences among the cultivars and correlate them to COVID-19 inhibitory activities allowing to pinpoint possible biomarkers. Further *in-vitro* and *in-vivo* studies are required to verify their activity.

1. Introduction

COVID-19 is a respiratory illness caused by the infection of severe acute respiratory syndrome coronavirus 2 (SARS-CoV-2). This febrile respiratory illness initially appeared in China in December 2019, then declared by the World Health Organization (WHO) as pandemic in March 2020, which rapidly spread globally in creepy rates (Fuzimoto and Isidoro, 2020). This life-threatening outbreak has brutally affected governments and health care systems around the world reaching over 72 million infections and more than 1.6 million confirmed deaths in late 2020 (Huang et al., 2021). In spite of increasing vaccine development, to date, there are few universally recommended therapies for SARS-CoV-2. One of these therapies is remdesivir which is approved by the Food and Drug Administration (FDA). It is a nucleotide prodrug of an adenosine analog. It binds to the viral RNA-dependent RNA polymerase and blocks viral replication by ending RNA transcription prematurely (Beigel et al., 2020). Owing to the shortage of the FDA approved anti-COVID-19 drugs, scientists are motivated to discover new ones (Xiong et al., 2020).

Historically, traditional herbal medicine has played a crucial role in the treatment and prevention of many diseases and infections (Xiong et al., 2020). Recently, phytochemical investigations by advanced scientific techniques were conducted in order to unveil various medicinal effects and pharmacological properties. Accordingly, a series of studies including systematic reviews, meta-analyses and clinical trials were focused on the imperative role of herbs in treating COVID-19. Some researches proved the effectiveness of combining herbs with synthetic drugs as an integrative treatment approach aiming to decrease the doses and side effects of the used synthetic drugs (Fuzimoto and Isidoro, 2020). They showed stunning role in elevating body immunity towards pathogens, reducing exaggerated inflammatory responses, and promoting body repair (Alam et al., 2021).

Lantana camara L. (Verbenaceae), commonly known as wild or red sage, is the most widespread species of genus *Lantana*. It is an ornamental woody straggling plant with various flower colors; red, pink, white, yellow and violet (Saxena et al., 2012). It is native to tropical regions of America and Africa. Many cultivars and hybrids of *L. camara* are cultivated and distinguished morphologically, physiologically and genetically (Negi et al., 2019). *L. camara* is reported for its ethnopharmacological uses. It is still medicinally used in different countries such as, Brazil, India, Kenya, Thailand, Mexico, USA, Tanzania, Nigeria, Indonesia, Australia, Canary Island and Southeast Asia. Leaves are used as anti-rheumatic, anti-catarrhal, anti-malaria, anti-cancer as well as to treat several viral disorders such as chicken pox, measles, cold, flu and whooping cough. In addition, they are used for treatment of asthma, fever, digestive disorders and eczema (Negi et al., 2019; Ross, 2003). The whole plant is used as tonic, carminative, to cure bronchitis, skin and mucosa sores, infections, ulcers and bruises (Negi et al., 2019; Ross, 2003). Recently, several research studies have been carried out to afford deep understanding to its pharmacological activities. For instance, different varieties of *L. camara* leaves and flowers are reported for antibacterial, anti-fungal, larvicidal, anti-ulcerogenic, hypoglycemic and anti-inflammatory activities (Kalita et al., 2012).To the best of our knowledge, only one study adopted by R. Kanagavalli et al. verified satisfactory anti-viral activity of both stems and flowers against polio virus type I (Kanagavalli et al., 2011). However, another research reviewed the inhibitory effect of its leaves to influenza virus A/Puerto Rico/8/34 (PR8) (Hasan, 2017). So far, no previous emphasis on the plant's probable COVID-19 inhibitory effects has raised, hence, prompted a growing interest in discovering more about its constituents.

Metabolomics is a branch of science intended for studying metabolites within living organisms and evaluating the changes in metabolic responses to physiopathological stimuli and genetic modifications (Puig-Castellví et al., 2020). It is considered as a helpful tool for standardization and quality control of herbs (Banerjee et al., 2021b). Metabolic profiling is a sub-class of metabolomics that could be attained using high-performance liquid chromatography coupled to mass spectrometry (HPLC or UPLC -MS). It can facilitate identification of either new compounds from plants or those that have previously isolated in a fast and accurate manner (Borges et al., 2019). Another worth mentioning sub-class is metabolic fingerprinting which is an unbiased screening approach that categorizes samples based on metabolic patterns (fingerprints) using mathematics and statistics. These patterns are vulnerable to changes in environmental, geographical or genetic conditions, hence, can determine discriminating metabolites (Dettmer et al., 2007). The study in hand is considered as the first study that applied UPLC-MS/MS to compare the chemical profiles of *L camara* cultivars. Multivariate analysis is the hallmark of metabolic fingerprinting to identify discriminating features to be forwarded to targeted analyses (Worley and Powers, 2013). Integrating both metabolic profiling and fingerprinting would afford simultaneous identification of metabolites, comparison of different metabolic patterns with respect to variable conditions and correlating them with biological activity (Dettmer et al., 2007).

Previous phytochemical analysis of *L. camara* revealed constituents of various chemical classes including flavonoids, anthocyanins, coumarins, lignans, iridoids, alkaloids, furanonaphthoquinones, saponins and triterpenoids. Recently, a surge in research on these endogenous metabolites has been conducted on account to their notable pharmacological activities and medicinal values (El Gendy, 2019). This urged exploring of the metabolic profiles of different plant varieties and identifying useful biomarkers responsible for their striking biological activities.

In the view of molecular virology, SARS-CoV-2 is an enveloped virus that belongs to family *Coronaviridae* (Payne, 2017). It contains single positive-stranded RNA and replicates inside the cytoplasm of human cell. SARS-CoV-2 comprises a genome sequence ranging from 26 to 32 kilobases and encodes for several structural and non-structural proteins (El-Hoshoudy, 2020). Structural proteins enclose the entire viral structure and are involved in its attachment to the host cell surface ex: the nucleocapsid protein, spike (S) protein, envelope (E) protein, membrane (M) protein (Peele et al., 2020). Envelope (E) protein is the smallest integral membrane protein in the viral lipid layer constituting 76 amino acids (Mohideen, 2021). It encompasses a short hydrophilic amino-terminus followed by a hydrophobic region and a hydrophilic carboxy-terminus (DeDiego et al., 2011). E protein is involved in viral virulence and facilitates viral morphogenesis during viral assembly and attachment to host cell membrane (Schoeman and Fielding, 2019). In addition, oligomerization of this protein leads to generation of ion channels (Narkhede et al., 2020). However, the virus encodes 16 non-structural proteins (nsp1 to nsp16), among which are protease (nsp5) and RNA-dependent RNA polymerase RdRp (nsp12) that is responsible for RNA synthesis (Roe et al., 2021). Recognizing such targets may open many gateways to the discovery of novel natural SARS-CoV-2 inhibitors (Zhao et al., 2021). Recent studies have proved the efficacy of phytoconstituents as anti-COVID-19 agents through several other mechanisms including inhibition of microtubules and

downregulation of angiotensin-converting enzyme 2 (ACE2) receptor anchorage precluding viral replication (Alam et al., 2021).

Owing to the scanty literature information concerning the anti-viral activity of *L. camara* against respiratory viruses, despite its historical role in treating various respiratory ailments, rapid flare up of COVID-19 mortality rates together with the inadequate availability of true therapeutic viricidal drugs, motivation was provoked to unravel its possible COVID-19 inhibitory effects which have not been previously investigated. This study aimed to investigate the chemical profiles of different *L. camara* cultivars using ultra performance liquid chromatography/tandem mass spectrometry (UPLC-MS/MS). Then, chemometric tools were implemented for detecting and guiding the refinement of anti-COVID-19 metabolites in the extracts. These biomarkers were then docked into the active site of potential targets in order to investigate their possible molecular mechanisms of action.

2. Materials and methods

2.1. Reagents, cell lines and apparatus

HPLC grade acetonitrile, formic acid, fetal bovine serum (FBS), dimethylsulfoxide (DMSO), L-glutamine, sodium pyruvate, sodium bicarbonate, sterile phosphate buffer saline (PBS), formalin (37% formaldehyde), crystal violet, isopropanol, HCl, Dulbecco's modified eagle medium (DMEM), 3-(4,5-dimethylthiazol-2-yl)-2,5-diphenyltetrazolium bromide (MTT), 98% purity were procured from Sigma–Aldrich (St. Louis, MO, USA).

The cell line used in this study was African green monkey renal epithelial cells (Vero E6, ATCC CRL-1586), purchased from American Type Culture Collection (Manassas, VA, USA). Cell culture plates, sterile tissue culture multi-well plates and culture flasks were obtained from Bio Whittaker, Lonza Group Ltd (Basel, Switzerland). Ultrasonic water bath (3 L Alpha Plus, Japan) and rotary evaporator (Rotavap Buchi 461) were utilized.

2.2. Collection of Lantana camara L. cultivars

Fresh flowers and leaves of *L. camara* cultivars named: Spreading sunset, Chelsea gem, Nivea and Drap d'or were collected in February 2021, from Antoniades Garden, Alexandria, Egypt (the latitude and longitude coordinates are 31.205924246975982 and 29.946966611257608, respectively). The authenticity of the plants was confirmed by Dr. Therese Labib, specialist of plant identification in El Orman Garden, Cairo, Egypt. Voucher specimens for cultivars (LC-250, LC-251, LC-252 and LC-253, respectively) were deposited at the herbarium of the Department of Pharmacognosy, Faculty of Pharmacy, Alexandria University. Flowers and leaves parts of each cultivar were left for complete dryness at room temperature.

2.3. Preparation of Lantana camara L. extracts

The air-dried powdered flowers and leaves from each cultivar (500 g each) were separately extracted by sonication in 1L of 95% ethanol (which is the universal solvent for extraction of almost all constituents of different chemical classes in the plant material) in an ultrasonic bath apparatus 28 kHz/1100 W for 30 min at 35 °C. The obtained extracts were filtered, and the procedure was repeated twice. The obtained extracts were combined and evaporated to dryness under reduced pressure using rotary evaporator at 45 °C. Each extract yielded about 200 g dry residue (Vinatoru et al., 1997).

2.4. Analysis of Lantana camara L. extracts using UPLC-MS/MS

2.4.1. Preparation of samples for UPLC-MS/MS analysis

All samples were prepared at concentration of 1 mg/mL using HPLC-grade methanol as a solvent. This concentration was selected after several trials, and it was found to be the best one that afforded the best resolution with maximum number of separable peaks. The prepared solutions were filtered using membrane disc filter (0.2 μm). Degassing of the solutions were done by sonication prior to injection. The full loop injected volume of each sample that was applied onto the chromatographic column was 10 μL.

2.4.2. Conditions of UPLC analysis

Secondary metabolites present in the leaves and flowers extracts of *L. camara* cultivars were determined using an UPLC XEVO TQD triple quadruple instrument Waters Corporation, Milford, MA01757 U.S.A. The chromatographic system was comprised of a Waters Acquity QSM pump, a LC-2040 autosampler, degasser in addition to Waters Acquity CM detector. The dimensions of Waters Acquity UPLC BEH C18 column that was used for the chromatographic separation were: 50 mm (length), 2.1 mm (internal diameter) and 1.7 μm (particle size). The operation of the column was at a flow rate of 0.2 mL/min and the system was thermostated at 30 °C.

The mobile phase, that was used for analysis, was composed of two phases; phase A and B. Phase A was composed of ultrapure water +0.1% formic acid, while phase B consisted of methanol +0.1% formic acid. These mobile phase components were used in order to provide good separation and resolution for the compounds. Moreover, 0.1% formic acid is a suitable solvent regarding MS detectors, as it shows a distinct influence on the responses and ionization efficiency of analytes (Alberti-Dér, 2013). Elution was a gradient one and its program was as following: 0.0–2.0 min, 10% B; 2.0–5.0 min, 30% B; 5.0–15.0 min, 70% B; 22.0min, 90% B; 22.0–25.0 min, 90% B; 26.0 min, 100% B; 26.0–29.0 min, 100% B; 30.0 min, 10% B; followed by 4 min to re-equilibrate the column.

2.4.3. Conditions of ESI-MS

Negative ionization mode was the mode in which samples were analyzed because it appeared more selective and sensitive for the LC-MS analysis of secondary metabolites in the extracts. Moreover, more observable peaks and a wide range of structural information were obtained in the negative mode in comparison to the positive one (Fabre et al., 2001). The analysis was carried out using a triple quadrupole (TQD) mass spectrometer coupled to electrospray ionization (ESI) source. The mass analyzer used was triple quadrupole (QqQ); it is used for tandem MS methods as its first and third quadrupoles act as filters of masses, while its second quadrapole, which is a radiofrequency-only quadrupole, is considered as a collision cell where parent ions are fragmented as a result of the interaction with a collision gas. QqQ is considered as a powerful tool for providing highly discriminating and many important structural data for the ions of compounds of interest (Ghallab et al., 2020).

ESI was operated at the following conditions: the capillary and cone voltages were set at 3 kV and 35 V, respectively. The ion source temperature was set at 150 °C and the pressure of the nitrogen gas (nebulizer) was adjusted at 35 psi. The temperature of drying and sheath gas (N_2) were 440 and 350 °C, respectively. The flow rates of the drying and sheath gas were adjusted at 900 and 50 L/h, respectively. The total run time of the analysis was 30 min. In order to achieve MS spectra, full range acquisition covering 100–1000 m/z was applied. Regarding automatic MS/MS fragmentation analyses of the parent ions, the first quadrupole (Q1) was used for mass-selection of parent ions. Collision-induced dissociation (CID) technique was used for the fragmentation of parent ions in the second quadrupole (Q2) using energy ramp from 30 to 70 eV by the use of collision gas (nitrogen gas). Finally, monitoring of the daughter ions yielded from the fragmentation was carried out in the third quadrupole. These ions were related to the molecular structure of the parent ions. Furthermore, MS^n experiments included the same conditions of chromatography and mass spectrometry as described above.

2.4.4. Annotation of UPLC-MS/MS metabolites

Assignment of the metabolites was accomplished by comparison of their retention times to external standards. Furthermore, quasi-molecular ions in addition to the characteristic MS/MS fragmentation pattern were used for metabolite annotation in comparison to our in-house database, reference literature and phytochemical dictionary of natural products database (CRC) in order to get metabolite annotation with a high level of confidence.

2.5. Multivariate statistical analysis

SIMCA-P ver 14.0 software (Umetrics, Sweden) was used for multivariate data analysis, including unsupervised pattern recognition; principal component analysis (PCA) and supervised pattern recognition; orthogonal projection to latent structures analysis (OPLS).

The UPLC-MS/MS data matrix (X-variables) was subjected to principal component analysis (PCA) in order to explore the clustering pattern, similarities and dissimilarities between different *L. camara* cultivars extracts based on their chemical profiles as well as to determine the chemical markers that are responsible for samples segregation. The UPLC-MS/MS results (X-variables) and the results of anti-COVID-19 activity (Y-variables) were subjected to orthogonal projection to latent structures (OPLS) analysis in order to investigate the clustering pattern of *L. camara* samples based on their anti-COVID activity so as to unravel the biomarkers related to such activity. The X and Y variables used for constructing the chemometric models are attached as a supplementary material (Table S1).

2.6. In vitro antiviral activity (cytotoxicity and plaque reduction assay)

2.6.1. Cytotoxicity of the tested extracts on Vero E6 cells

Before conducting plaque reduction assay, it was a must to assess the cytotoxicity of the tested extracts on normal Vero E6 to ensure their safety. According to Mosmann's test (MTT test), A tetrazolium salt; MTT (3-(4,5-dimethylthiazol-2-yl)-2,5-diphenyl tetrazolium bromide) has been used to develop a rapid quantitative colorimetric assay for mammalian cell survival and proliferation. The assay detects living, but not dead cells and the signal generated is dependent on the degree of activation of the cells. This method can therefore be used to measure cytotoxicity (Mosmann, 1983). The dilution of the tested extracts was done with Dulbecco's Modified Eagle's Medium (DMEM). The stock solutions of the tested extracts were prepared in 10% DMSO in double distilled H_2O and serial dilutions were prepared from it in order to keep DMSO concentrations in the range of (0.1–0.5%) to ensure the safety of the treated cells from the cytotoxic effect of DMSO. MTT method with minor modifications was used to evaluate the cytotoxic effects of the tested extracts on Vero E6 cells (Mosmann, 1983). In 96 well plates, Vero E6 cells were seeded (100 μL/well at a density of 3×10^5 cells/mL) and incubated for 24 h at 37 °C in 5% CO_2. After 24 h, treatment of cells with various concentrations of the tested extracts (6.25, 12.5, 25, 50 and 100 μg/mL) in triplicates was done. These extracts concentration levels were chosen by referring to Mossman's test (Mosmann, 1983). Then these cells treated with different extracts concentrations were incubated for another 24 h. After that, the supernatant layer was discarded, and washing of cell monolayers with sterile PBS three times was carried out. To each well, MTT solution (20 μL of 5 mg/mL stock solution) was added, followed by incubation at 37 °C for 4 h then medium aspiration was carried out. The formed formazan crystals were dissolved with 200 μL of acidified isopropanol (0.04 M HCl in absolute isopropanol, 0.073 mL HCl in 50 mL isopropanol). Finally, a multi-well plate reader was used to measure the absorbance of formazan solutions at λ_{max} 540 nm using 620 nm as a reference wavelength. The percentage of cell cytotoxicity compared to the untreated cells was calculated with the following equation:

$$\% \ CC_{50} = ((A_0\text{-}A)/A_0) \ *100$$

A_0 is the absorbance of cells without treatment.

A is the absorbance of cells with treatment.

CC_{50}, which is the drug concentration required for reducing the cell viability by 50%, was determined by plotting % cytotoxicity versus sample concentrations (Civitelli et al., 2014).

2.6.2. Anti-COVID-19 activity using plaque reduction assay

Vero E6 cells (1×10^6 cells/mL) were cultivated in a six well plate for 24 h at 37 °C. Dilution of SARS-CoV-2 (COVID-19) was done to give 1×10^4 plaque-forming unit (PFU)/well, followed by mixing with 100 μL of the safe concentrations of the tested extracts (30, 15, 12.5 and 6.25 μg/mL) and incubated for 1 h at 37 °C before being added to the cells. After that, removal of growth medium from the cell culture plates was carried out followed by cell inoculation with the tested extracts. Virus adsorption was done for 1 h contact time followed by addition of 3 mL of DMEM (supplemented with 2% agarose), the tested extracts and virus onto the cell monolayer. Plates were left to solidify then incubated at 37 °C till formation of viral plaques (3 days). Formalin (10%) was added for 2 h then plates were stained with 0.1% crystal violet in distilled water. Untreated virus incubated with Vero E6 cells were considered as control wells. Finally, the percentage reduction in plaques formation (% reduction) in comparison to control wells was recorded by counting plaques using the following equation:

$$\% \ \textbf{Reduction} = ((\text{viral count (un)} - \text{viral count (t)})/\text{viral count (un)}) \ *100$$

Viral count (un) is the viral count in wells where virus was untreated with the extracts.

Viral count (t) is the viral count in wells where virus was treated with the extracts.

% Reduction values and their corresponding concentration values were subjected to non-linear regression analysis via GraphPad Prism® version 8 (GraphPad Software Inc., San Diego, CA, USA) (https://www.graphpad.com) to generate sigmoidal dose-response curves, from which the concentration causing 50% viral count reduction (IC_{50}) was extrapolated (Civitelli et al., 2014).

The selectivity indices that measure the window between the cytotoxicity and antiviral activity (Indrayanto et al., 2021) of the tested extracts were calculated according to the following equation:

Selectivity index = (CC_{50} of the extract on normal Vero E6 cells/IC_{50} of the extract on infected Vero E6 cells)

2.6.3. Generation of SARS-CoV-2 cDNA

The Qiagen viral RNA-isolation kit (#52906) was used to extract RNA from 200 μL aliquots of sample supernatant or cell suspension. The extracted RNA was eluted in 60 μL. Moreover, the commercial first strand cDNA synthesis kit (Thermo Scientific, USA) was used to perform reverse transcription according to the manufacturer's instructions. Total reaction mixture (20 μL) was composed of 10 μL of RNA extract, 4 μL of 5x TransAmp buffer, 1 μL of Reverse Transcriptase and 5 μL of Nuclease free water. Incubation of the reactions were carried out at 25 °C for 10 min, 42 °C for 15 min and 85 °C for 5 min (Caly et al., 2020).

2.6.4. Analysis of COVID-19 RdRp and E genes expression using a TaqMan real-time RT-PCR assay

BetaCoV RdRp gene and BetaCoV E-gene were amplified using the following sets of primers and probes. Regarding BetaCoV RdRp gene, 1 μM forward (5'- AAA TTC TAT GGT GGT TGG CAC AAC ATG TT-3'), 1 μM reverse (5'- TAG GCA TAG CTC TRT CAC AYT T-3') primers and 0.2 μM probe (5'-FAM- TGG GTT GGG ATT ATC-MGBNFQ-3') (Abcam, UK) were used. However, in BetaCoV E-gene, 1 μM forward (5'-ACA GGT ACG TTA ATA GTT AAT AGC GT -3'), 1 μM reverse (5'-ATA TTG CAG CAG TAC GCA CAC A-3') primers and 0.2 μM probe (5'-FAM-ACA CTA GCC ATC CTT ACT GCG CTT CG- 286 NFQ-3') (Abcam, UK) were used

(Corman et al., 2020). Real-time RT-PCR assays were carried out on an Applied Biosystems ABI 7500 Fast real-time PCR machine (Applied Biosystems, Foster City, CA, USA), and the cycling conditions were: 95 °C for 2 min, 95 °C for 5 s, 60 °C for 24 s. SARS-CoV-2 cDNA (Ct~28) was used as a positive control. Threshold cycle (Ct) values were calculated and converted to fold-reduction of treated samples compared to control using the ΔCt method (fold changed in viral RNA = $2^{\hat{}}\Delta Ct$) which is a simple formula that used for the calculation of the relative fold gene expression of samples. RdRp and E genes expression was expressed as % down regulation (Caly et al., 2020). The tested extracts effects on the genes expression were measured at four levels of the extracts' safe concentrations (30, 15, 12.5 and 6.25 μg/mL).

2.7. Molecular docking studies

Molecular docking studies were performed using Glide module integrated in Schrodinger software. The Protein Data Bank (PDB) was utilized to retrieve the crystal structure of RdRp protein (PDB ID: 6M71), which was retrieved as pdb file for further preparation using the PrepWiz module. Preprocessing of the protein's structure was first attained through assignment of bond orders and H atoms to the structure (loops). Further, Water molecules beyond 5 Å from the active site were removed and protonation states were determined. After modification and reviewing, hydrogen bonds were assigned using PROPKA at PH = 7 followed by energy minimization using OPLS 3 force field until the relative mean standard deviation (RMSD) of the minimized structure compared to the crystal structure exceeded 0.30 Å. Defining of the active site was determined using the receptor grid generation module where the boxes enclosing the centroids of co-crystallized ligands were set as the grids with a size adjusted to ≤20 Å. The residues Asp618, Ser759, Asp760, Asp761, Asp623, Arg555, Arg 553, Lys 545, Val557, Ser682, Asn691, Thr680 were used for receptor grid generation, as assigned from literature (Tiwari, 2021).The grid box x, y, and z coordinates were 113.45, 114.89, and 123.36, respectively. The size of grid box was 30 × 30 × 30 $Å^3$. The 3D-structures of compounds to be docked were imported as SDF files to be prepared using Ligprep module which generated molecules with correct chiralities, ionization states, tautomers, stereochemistries and ring conformations. Subsequently, geometry minimization was carried out for all the prepared ligands by means of OPLS 3 force field. Docking simulations were performed using GLIDE module. The generated compounds from the LigPrep file were flexibily docked using extra precision (XP) docking. 2D and 3D ligand-target interactions were investigated in maestro interface.

3. Results

3.1. Chemical profiling of the leaves and flowers extracts of Lantana camara L. cultivars using UPLC-MS/MS

The UPLC-MS base peak chromatograms of the hydroalcoholic extracts of the leaves and flowers of *L. camara* cultivars showed the presence of a total of 47 peaks (Figs. S1–S8). The identified compounds belong to different classes of secondary metabolites including flavonoids, phenolic acids, iridoid glycosides, phenylethanoid glycosides, lignan glycosides and triterpenes. Table 1 represents the data for the identified compounds including the name of the tentatively identified compounds, their retention times, *m/z* values, molecular formulas and their MS fragmentation patterns (matched within 25 ppm error tolerance).

Heat map (Fig. 1) showed that caffeic acid, isoverbascoside and pectolinarin are present in all the tested extracts with approximately the same high concentration. Whereas, luteolin-7,4'-O-diglucoside is common in all studied extracts but with variable amounts.

3.2. Investigation of the inter-cultivar effect on the metabolic profile using multivariate statistical analysis of the UPLC-MS/MS data

3.2.1. Unsupervised pattern recognition

The principal component analysis (PCA) score scatter plot (Fig. 2A) showed that flowers extracts are more consistent in their clustering than leaves extracts. Regarding flowers, their samples clustered along the positive side of PC1 except *L. camara* cv. Drap d'or that clustered along the negative side of the same principal component. This indicated that the inter-cultivar effect has no pronounced effect on the chemical profile of flowers extracts. However, leaves samples of *L. camara* cv. Drap d'or were clustered along the positive side of PC2, and *L. camara* cv Chelsea gem leaves samples were clustered along the negative side of the same principal component. Whereas, the remaining leaves samples clustered together with flowers samples along the positive side of PC1. These results indicated that *L. camara* cv. Drap d'or and *L. camara* cv Chelsea gem leaves held a greater variability in their chemical profiles than other tested leaves extracts. Therefore, the inter-cultivar factor has a noticeable effect on the chemical profiles of leaves extracts.

From the loading plot (Fig. 2B), it can be observed that: *Cis*-verbascoside, linaloic acid hexoside, lamiridoside, dihydroxy-dimethoxy flavone hexoside II and III, and reduced lantadene A were the distinctive chemical components of *L. camara* cv. Drap d'or leaves extract. These compounds either exclusively present in this extract or exist in a higher concentration than other studied extracts. Therefore, they were considered as significant loadings to such extract. On the other hand, camarolic acid, lantacin, icterogenin, lantoic acid, camaranoic acid and lantabetulic acid were exclusively found in the extract of *L. camara* cv Chelsea gem leaves, thus by referring to the loading plot they were found to be significantly related to such samples. Furthermore, eupafolin, 8-epiloganin and protocatechuic acid were solely present in *L. camara* cv. Drap d'or flowers extracts thus, could act as distinctive loadings responsible for the discrimination of this extract from other flowers extracts.

3.3. Cytotoxicity and anti-COVID activity of the tested extracts

3.3.1. Assessment of the cytotoxicity of the tested extracts on Vero E6 cells

As depicted from Table 2, all the tested extracts showed 50% cytotoxicity (CC_{50}) at concentrations more than 30 μg/mL indicating their safety on these cells (Darwish et al., 2020).

3.3.2. Anti-COVID-19 activity using plaque reduction assay

All the tested extracts showed variable inhibitory effects on the viral plaques as observed from their IC_{50} values (Table 2). Among the tested extracts, leaves and flowers extracts of *L. camara* cv Chelsea gem, flowers extracts of *L. camara* cv Spreading sunset and *L. camara* cv Drap d'or were the most promising inhibitors to viral plaques as they exhibited IC_{50} values of 3.18, 3.67, 4.18 and 5.01 μg/mL, respectively. On the contrary, the flowers extract of *L. camara* cv Nivea showed the highest IC_{50} value (15.05 μg/mL) among the tested extract, thus can be considered as the least active extract against COVID-19. In addition, flowers and leaves extracts of *L. camara* cv Chelsea gem, flowers extracts of *L. camara* cv Spreading sunset and *L. camara* cv Drap d'or showed the highest selectivity indices scoring 12.3, 10.1, 8.6 and 7.8, respectively, indicating their relative high safety and efficacy (Table 2).

3.3.3. Effects of the tested extracts on expression of SARS-CoV-2 RdRp and E genes

By analyzing the effect of the different cultivars extracts on expression levels of SARS-CoV-2 RdRp and E genes, it was observed that all of them demonstrated a dose-dependent inhibition with exception of *L. camara* cv Chelsea gem. It was also found that inhibiting the expression of RdRp gene is the major mechanism behind the antiviral activity of all extracts at almost all concentration levels. At the concentration of 30 μg/mL, the tested extracts showed % downregulation of RdRp gene in

Table 1
Metabolites identified in the extracts of *L. camara* cultivars using UPLC-MS/MS in negative ionization mode.

Peak number	Rt (min)	Identified compounds	M-H	Molecular weight	Chemical class	Element composition	Major fragments
1	1.4533	luteolin-7, 4'-O -diglucoside	609	610	Flavonoids	C27H26O18	447, 285, 137, 151, 241
2	1.49	Protocatechuic acid	153	154	Phenolic acids	C7H6O4	109
3	1.6	Caffeic acid	179	180	Phenolic acids	C9H8O4	135
4	1.6733	Fucatoside B	741	742	Phenylethanoid glycosides	C33H42O19	179, 161, 579, 447, 315, 135
5	1.7338	Theveside	389	390	Iridoid	C16H22O11	227, 345, 371
6	2.01	Vanillic acid	167	168	Phenolic acids	C12H6O4	151, 123
7	2.2433	Fucatoside C	741	742	Phenylethanoid glycosides	C33H41O19	179, 161, 447, 579, 315, 135
8	2.88	Coumaric acid	163	164	Phenolic acids	C9H8O3	119
9	2.99	Ferulic acid	193	194	Phenolic acids	C10H10O4	149
10	3.1304	Ethyl-β-D- galactoside	207	208	Aliphatic glucosides	C8H16O6	45
11	3.6	Lamiridoside	421	422	Iridoid	C17H26O12	391, 259, 361, 343
12	4.7	8-epiloganin	389	380	Iridoid	C17H26O10	359, 227, 329, 311
13	5.10	Linaloic acid hexoside	345	346	Aliphatic acid glycoside	C16H26O8	183, 301, 327
14	13.232	Pectolinarin	621	622	Flavonoids	C29H34O15	314, 299, 284, 234
15	10.79	Radulignan	585	586	Lignan	C26H34O15	423, 570
16	10.967	Arenarioside	755	756	Phenyl ethanoid glycosides	C34H44O19	179, 161, 593, 135
17	11.076	Verbascoside	623	624	Phenyl ethanoid glycosides	C29H36O18	179, 161, 461, 315, 135
18	11.23	Cis-verbascoside	623	624	Phenylethanoid glycosides	C29H36O15	179, 161, 461, 315, 135
19	11.593	Isoverbascoside	623	624	Phenyl ethanoid glycosides	C29H36O16	179, 161, 461, 315, 135
20	12.173	Parvifloroside A	623	624	Phenyl ethanoid glycosides	C29H36O15	179, 161, 461, 315, 135
21	7.48	Dihydroxy-dimethoxy flavone hexoside I	491	492.14	Flavonoids	C23H24O12	329, 150, 299
22	12.36	Dihydroxy-dimethoxy flavone hexoside II	475	476	Flavonoids	C23H24O11	313, 283, 150
23	12.468	Dihydroxy-dimethoxy flavone hexoside III	475	476	Flavonoids	C23H24O11	313, 283, 134
24	13.51	3α,30-Diacetyloxy-12α-hydroxy-23-oxoeupha-7,24-dien-21,16β-olid-28-oic acid 28-O-β-D-glucopyranosyl ester	775	776	Eupha-type triterpene	C40H56O15	613, 715
25	15.31	Eupafolin	315	316	Flavonoids	C16H12O7	300, 181, 136
26	15.48	Cirsiliol	329	330	Flavonoids	C17H14O7	299, 195, 136
27	16.1	Lantalucratin F	333	334	Naphthoquinone	C17H18O7	318, 305, 277
28	17.56	5-Hydroxynaphtho[2,3-b]furan-4,9-dione	213	214	Furanonaphthoquinone	C12H6O4	185, 157
29	18.09	Salvigenin	327	328	Flavonoids	C18H16O6	282, 195, 134
30	21.85	3- acetyloxy,12-hydroxy-23-oxoeupha-7,24-dien-21,16-olid-28-oic acid	555	556	Eupha-type triterpene	C32H44O8	495, 511, 537, 540
31	22.22	Camarolic acid	583	584	Oleane-type triterpene	C35H52O7	467, 98, 423, 186, 245, 200
32	22.83	Camaric acid	567	568	Oleane-type triterpene	C35H52O6	451, 407, 98
33	23.17	Lantanilic acid	567	568	Oleane-type triterpene	C35H52O6	451, 407, 98
34	23.57	Lantacin	569	570	Ursane-type triterpene	C35H54O6	98, 453, 409
35	23.66	Icterogenin	567	568	Oleane-type triterpene	C35H52O6	451, 407, 98
36	24.12	Lantoic acid	485	486	Ursane-type triterpene	C30H46O5	437, 421, 407
37	24.33	Camaranoic acid	483	484	Ursane-type triterpene	C30H44O5	435, 419, 405, 391
38	24.66	Camarinic acid	527	528	Ursane-type triterpene	C32H48O6	58, 451, 407
39	26.71	Reduced lantadene A	553	554	Oleane-type triterpene	C35H54O5	98, 437, 393
40	27.1	3- O-(3-Methyl-2-butenoyl), 22-hydroxy-12-oleanen-28-oic acid;	553	554	Oleane-type triterpene	C35H54O5	98, 437, 393
41	27.43	Lantadene B	551	552	Oleane-type triterpene	C35H52O5	98, 435, 391
42	30.31	Lantaiursolic acid	555	556	Ursane-type triterpene	C35H56O5	537, 493
43	31.22	Pomonic acid	469	470	Ursane-type triterpene	C30H46O4	451, 407
44	32.21	Lantabetulic acid	469	470	Lupane-type triterpene	C30H46O4	425, 451, 222, 220, 175
45	32.33	Lantanolic acid	469	470	Oleane-type triterpene	C30H46O4	421, 391, 420, 377
46	33.21	Lantic acid	469	470	Ursane-type triterpene	C30H46O4	421, 391, 420, 377
47	34.71	Camardienone	437	438	Oleane-type triterpene	C29H42O3	174, 186, 215

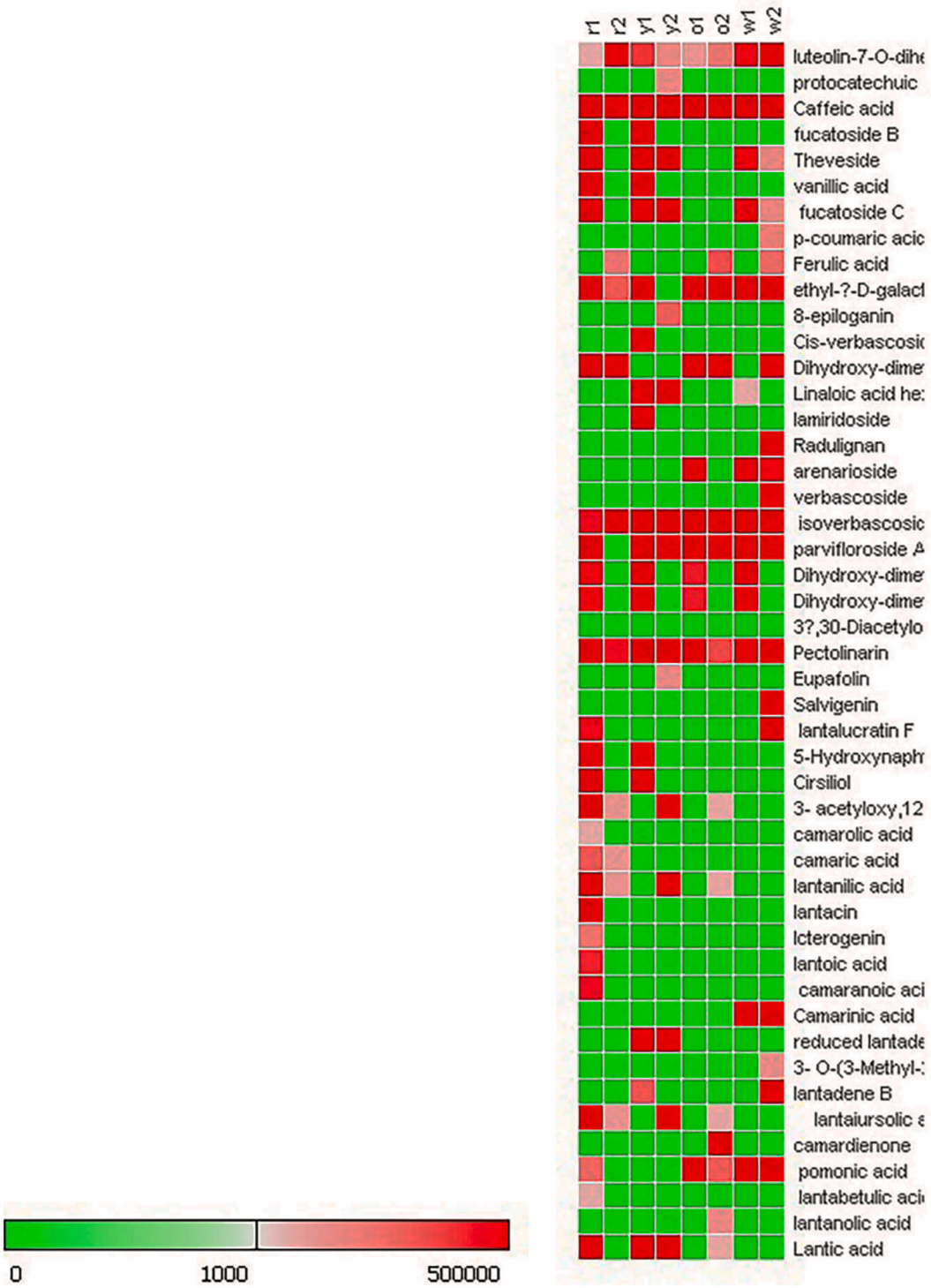

Fig. 1. Heat map of all identified metabolites in tested extracts of *L. camara*; (r1) Chelsea gem cultivar leaves, (r2) Chelsea gem cultivar flowers, (y1) Drap d'or cultivar leaves, (y2) Drap d'or cultivar flowers, (O1) Spreading sunset cultivar leaves, (O2) Spreading sunset cultivar flowers, (w1) Nivea cultivar leaves and (w2) Nivea cultivar flowers. (Red and green colors indicate high and low abundances, respectively). Heat map was constructed using Gitools program (http://www.gitools.org/download) based on the total ion current values of the identified mass fragments.

a range of (87.48%–99.99%) (Fig. 3). Furthermore, at the concentration of 6.25 μg/mL, leaves and flowers extracts of *L. camara* cv Nivea and *L. camara* cv Chelsea gem showed % downregulation values of RdRp gene of 69.22, 60.81, 54.62 and 60.33, respectively, indicating that these extracts were the most active ones regarding inhibiting the RdRp gene expression. On the other hand, leaves and flowers extracts of *L. camara* cv Spreading sunset and *L. camara* cv Drap d'or downregulated E gene by (46.41%, 70.19%, 35.05% and 65.92%, respectively) at the concentration of 6.25 μg/mL, thus these extracts were considered as the most active ones regarding downregulating E gene. Moreover, flowers extract of *L. camara* cv Chelsea gem showed anti-COVID-19 activity mainly through equivalent inhibition of both E and RdRp genes expressions (60.82 and 60.33%, respectively) at the concentration of 6.25 μg/mL.

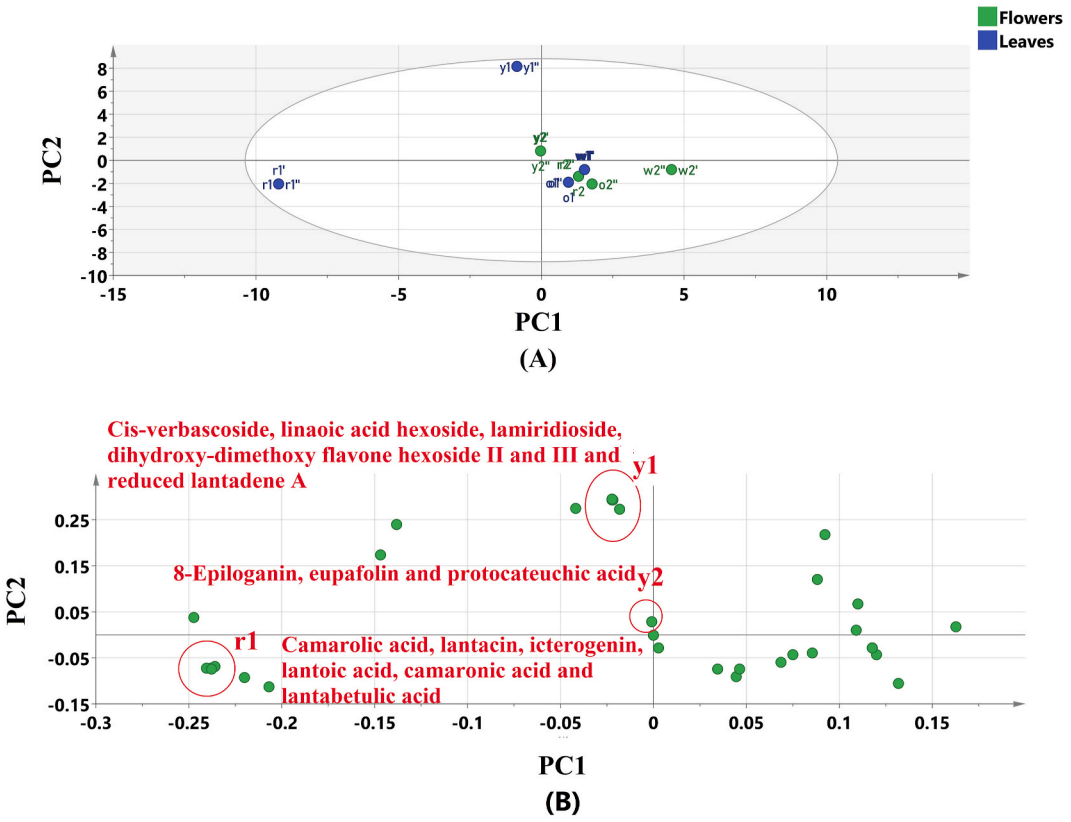

Fig. 2. PCA score plot of different *L. camara* cultivars extracts (A). Loading plot showing important loadings responsible for r1, y1 and y2 samples segregation (B).

Table 2
CC_{50}, IC_{50} and selectivity indices values for the different *L. camara* cultivars.

Cultivar	CC_{50} (MTT assay) μg/mL	IC_{50} (Plaque reduction assay) μg/mL	Selectivity factor
L. camara cv Spreading sunset leaves	40	8.751	4.6
L. camara cv Spreading sunset flowers	36	4.188	8.6
L. camara cv Chelsea gem leaves	32	3.181	10.1
L. camara cv Chelsea gem flowers	45	3.671	12.3
L. camara cv Nivea leaves	32	6.820	4.7
L. camara cv Nivea flowers	32	15.05	2.1
L. camara cv Drap d'or leaves	32	8.715	3.7
L. camara cv Drap d'or flowers	39	5.015	7.8

3.4. Determination of the anti-COVID-19 biomarkers using supervised pattern recognition analysis

The score scatter plot (Fig. 4A) showed the in-between class discrimination along PC1 between leaves and flowers extracts of *L. camara* cv Chelsea gem, flowers extracts of *L. camara* cv Spreading sunset and *L. camara* cv Drap d'or which clustered along the positive side of PC1 and leaves and flowers extracts of *L. camara* cv Nivea, leaves extracts of *L. camara* cv Spreading sunset and *L. camara* cv Drap d'or that clustered along the negative side of the same principal component. Hierarchical analysis confirmed these results, as the dendrogram (Fig. 4B) showed two main clusters A and B. Cluster A included leaves and flowers extracts of *L. camara* cv Chelsea gem, flowers extracts of *L. camara* cv Spreading sunset and *L. camara* cv Drap d'or, while cluster B was composed of leaves and flowers extracts of *L. camara* cv Nivea, leaves extracts of *L. camara* cv Spreading sunset and *L. camara* cv Drap d'or. The reason behind such clustering and segregation was that cluster A extracts showed a higher anti-COVID-19 activity and lower IC_{50} values than those of cluster B extracts.

In addition, coefficient plot (Fig. 5) showed the twelve biomarkers (positive contributors) associated with COVID-19 inhibitory activity of the studied extracts. These biomarkers were camaric acid, ferulic acid, isoverbascoside, lantanilic acid, lantiursolic acid, luteolin-7,4'-O-diglucoside, lantabetulic acid, camarolic acid, icterogenin, camaranoic acid, lantacin and lantoic acid.

3.5. Molecular docking studies on the biomarkers

As depicted in Table 3, the tested compounds interact with different binding affinities with the active site of SARS-COV-2 RdRp gene and were ranked based on their XP Gscore as follows: isoverbascoside > luteolin-7, 4'-O -diglucoside > camarolic acid > lantoic acid > lantaiursolic acid > lantanilic acid > ferulic acid > camaric acid > lantabetulic acid > lantacin > icterogenin > camaranoic acid. Surprisingly, it was noted that isoverbascoside, luteolin-7,4'-O-diglucoside, camarolic acid and lantoic acid exhibited higher docking scores of −11.378, −10.64, −6.72 and −6.07 kcal/mol, respectively, when compared to remdesivir (−5.75 kcal/mol), reflecting their higher binding affinity to SARS-CoV-2 RdRp gene. Therefore, they can serve as promising lead compounds or candidates for discovery of novel and potent COVID-19 inhibitory drugs with lower side effects.

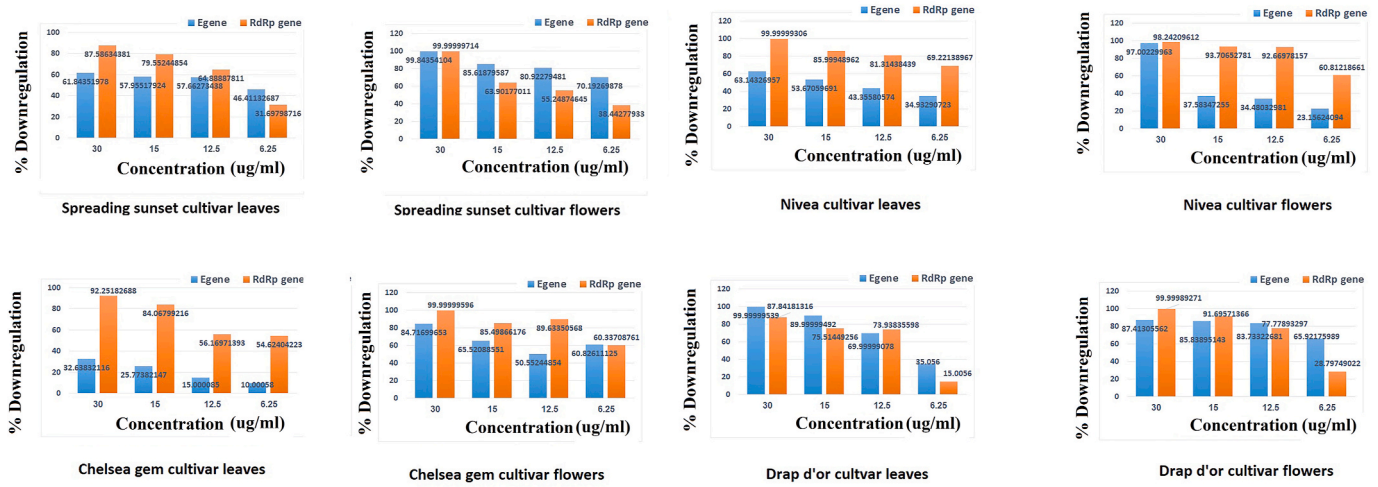

Fig. 3. Bar charts showing % downregulation of E gene (blue) and RdRp gene (orange) of different *L. camara* cultivars extracts.

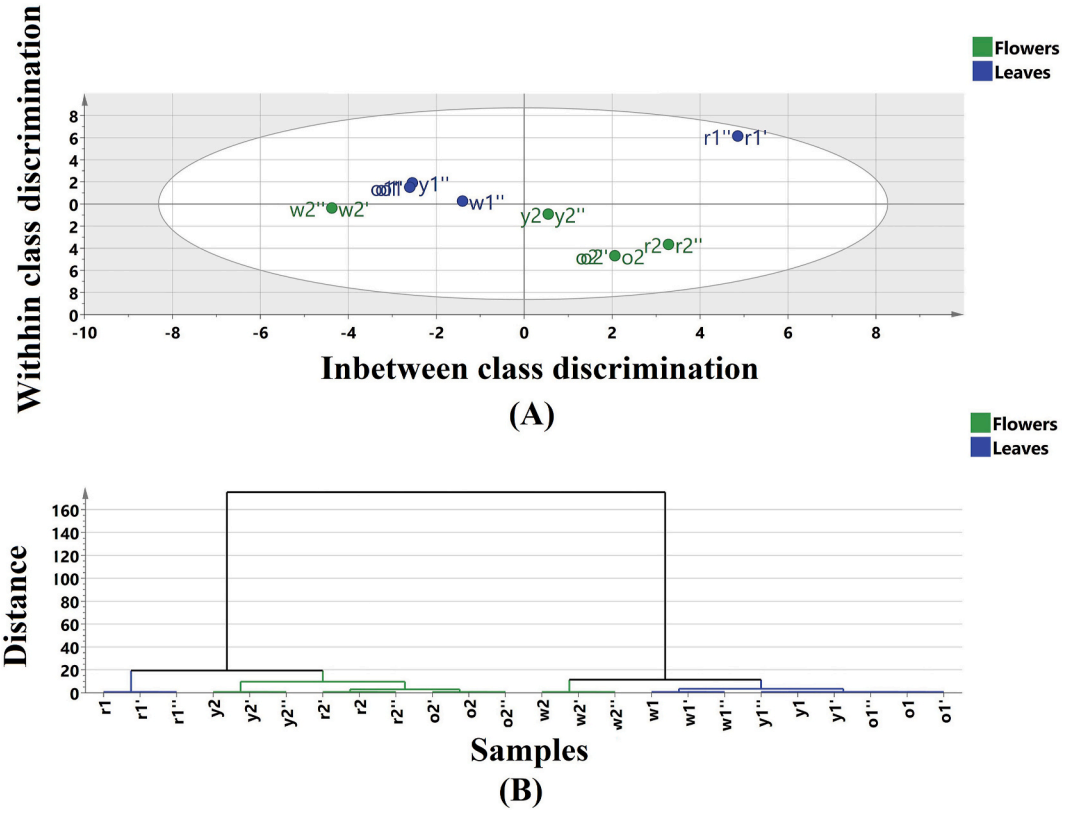

Fig. 4. OPLS score plot (A) and Hierarchical clustering analysis plot (B) of different *L. camara* cultivars extracts.

4. Discussion

4.1. Chemical profiling of the leaves and flowers extracts of Lantana camara L. cultivars using UPLC-MS/MS

UPLC-MS is an important tool utilized to unveil the differences in metabolic profiles among different *L. camara* cultivars (Soininen et al., 2014). MZmine software (2.53) was used for the extraction of the retention time, peak area, and MS/MS intensity of components from raw UPLC- MS/MS data.

Heat map (Fig. 1) was constructed using Gitools program (http://www.gitools.org/download) based on the total ion current values of the identified mass fragments. This heat map illustrates the relative amounts of the identified metabolites in each sample, and this is represented with varying color intensity from green (minimum quantity) to red (maximum quantity).

The identified metabolites belong to different chemical classes. Investigation of their chromatographic patterns and characteristic fragmentation pathways formerly illustrated in literature enabled to gain as much structural information as possible.

4.1.1. Triterpenes

Nineteen peaks (**24, 30–47**) were identified as triterpenes, among which 2 peaks (**24** and **30**) belong to euphane-type triterpene (Kikuchi

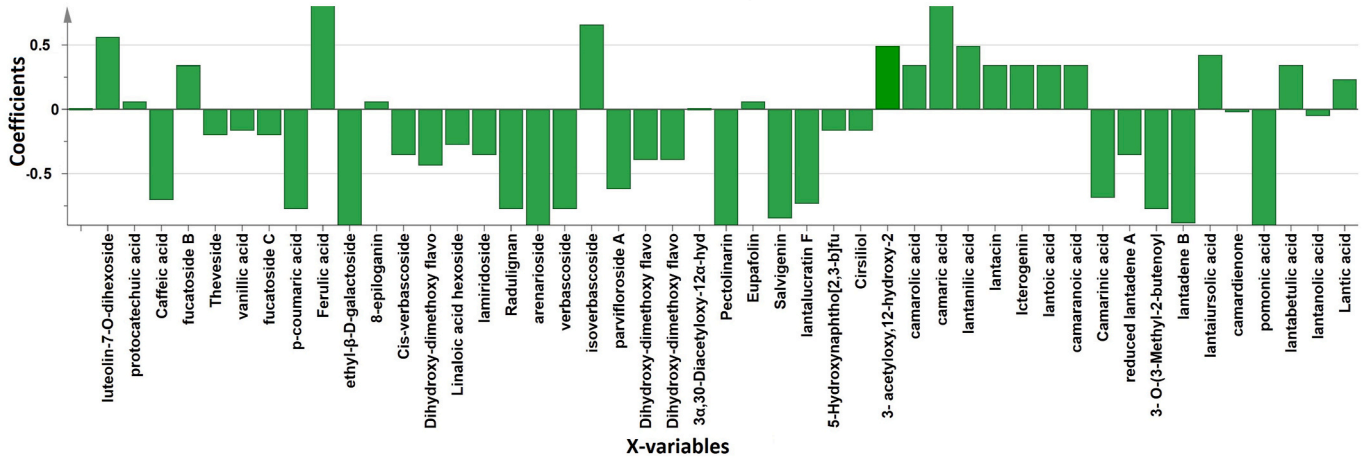

Fig. 5. Coefficient plot of OPLS model of anti-covid activity (plaque reduction assay).

Table 3
XP Gscores of the screened phytochemical biomarkers binding at the active site of SARS-CoV-2 RdRp gene expressed in kcal/mol.

Compound	Binding score (kcal/mol)
Isoverbascoside	−11.38
Luteolin-7, 4'-O -diglucoside	−10.64
Camarolic acid	−6.73
Lantoic acid	−6.07
Redemesivir	−5.75
Lantaiursolic acid	−3.867
Lantanilic acid	−3.633
Ferulic acid	−3.372
Camaric acid	−3.198
Lantabetulic acid	−2.958
Lantacin	−2.919
Icterogenin	−2.311
Camaranoic acid	1.272

et al., 2016). Compound **24** showed a quasi-molecular peak (M-H) at 775 Da, characteristic mass fragments at 613 Da (M-H-162) and 715 Da (M-H-120) due to loss of glucose unit and two acetate groups, respectively and it was tentatively identified as 3α,30-Diacetyloxy-12α-hydroxy-23-oxoeupha-7,24-dien-21,16β-olid-28-oic acid 28-O-β-D-glucopyranosyl ester. Furthermore, compound **30** showed a quasi-molecular ion peak at 555 Da and primarily yielded daughter ions at 495 Da (M-H-60), 511 Da (M-H-44), 537 Da (M-H-18) and 540 Da (M-H-15) due to the loss of acetate, CO_2, water and methyl group, respectively. This compound was tentatively identified as 3-acetyloxy, 12-hydroxy-23-oxoeupha-7,24-dien-21,16-olid-28-oic acid. Peak **44** exhibited a lupane-type triterpene nucleus and it showed characteristic mass fragments at 425 Da (M-H-CO_2), 451 Da (M-H-H_2O) (Ayatollahi et al., 2011). The corresponding compound was characterized as lantabetulic acid. The existence of significantly important daughter ions due to loss of angeloyl or methyl butenoyl or hydroxyl moiety followed by loss of CO_2 were displayed in the mass spectra of nine peaks (**31, 32, 33, 35, 39, 40, 41, 45** and **47**) belonging to oleane-type triterpenoids. By referring to literature, they are tentatively identified as, camarolic acid, camaric acid, lantanillic acid, icterogenin, reduced lantadene A, 3-O-(3-methyl-2-butenoyl), 22-hydroxy-12-oleanen-28-oic acid, lantadene B, lantanolic acid and camardienone, respectively (Ayatollahi et al., 2011; Begum et al., 2008, 2014; Chen et al., 2010). Finally, 7 peaks (peaks **34, 36, 37, 38, 42, 43** and **46**) were found to belong to ursane-type triterpenes. The most important mass fragments were due to loss of angeloyl or methyl butenoyl or hydroxyl moiety followed by loss of CO_2. These compounds were tentatively identified as lantacin, lantoic acid, camaranoic acid, camarinic acid, lantiursolic acid and lantic acid, respectively (Ayatollahi et al., 2011; Begum et al., 2008, 2014; Chen et al., 2010).

4.1.2. *Flavonoids*

Eight compounds were identified as flavonoids; among which 5 were identified as flavone glycosides (**peaks 1, 14, 21, 22, 23**) and 3 as methoxylated flavones (**peaks 25, 26, 29**). Compounds **1** and **14** were recognized to be diglycosides. Compound **1** was annotated as diglucoside from the MS^2 fragments at (M-H-162) and (M-H-162) that indicated the loss of two hexose units connected to two different positions of the aglycone (Brito et al., 2014). Furthermore, the MS^2 fragment at 429 Da indicated that the inter-glycosidic linkage was (1–2) linkage (Kachlicki et al., 2016). Meanwhile, the fragmentation pattern of compound **14** showed two characteristic MS^2 fragments (M-H-162) and (M-H-162-162) that indicated the loss of two sugar units at different substitution position of the aglycone unit (Ghallab et al., 2020). Compounds **21, 22** and **23** were deduced to be monoglycosides due to the presence of the MS^2 fragment (M-H-162) indicating the loss of a hexose unit (Kachlicki et al., 2016).

The aglycone part of flavonoids can be identified based on further MS^2 experiments with CE = 70 eV. Compound **1** showed characteristic mass fragments at 137 and 151 Da resulting from RDA (Retro-Diels Alder rearrangement) in addition to a mass fragment at 241 Da (M-H-CO_2). Based on these observations and by referring to the literature survey, it was tentatively identified as luteolin-7, 4'-O-diglucoside (Li et al., 2016). Compound **14** was identified as a di-methoxylated flavone, as deduced from the MS^2 fragment of its aglycone (M-H-$2CH_3$) at 299 Da (Zhao et al., 2020). After comprehensive analysis of the mass data with that reported in literature, compound **14** was identified as pectolinarin (Liao et al., 2018). Compounds **21, 22** and **23** exhibited a di-methoxylated flavone glucoside skeleton as all of them showed a mass fragment (M-H-$2CH_3$) at 299 Da. Compound **21** was tentatively identified as dihydroxy-dimethoxy-flavone hexoside I, showing characteristic RDA fragments at 181 Da ($MeA^{1,3}$) and at 150 Da ($MeB^{-0,2}$). That confirmed the presence of one methoxy and two hydroxy groups at ring A in addition to one methoxy and one hydroxy group in ring B. Meanwhile, compounds **22** and **23** were tentatively identified as dihydroxy-dimethoxy-flavone hexoside II and III displaying characteristic RDA fragments at 165 Da ($MeA^{-1,3}$), 150 Da ($MeB^{-0,2}$) and 181 Da ($MeA^{-1,3}$), 134 Da ($MeB^{-0,2}$), respectively. Those findings indicated that compound **22** possessed one methoxy and one hydroxy substituent in both rings A and ring B. On the other hand, compound **23** demonstrated a different substitution pattern with one methoxy and two hydroxy groups in ring A in addition to one methoxy group in ring B. Peaks **25, 26** and **30** corresponded to mono, di and tri-methoxylated flavone aglycones, respectively. This was inferred by the presence of the characteristic mass fragment 300Da (M-H-CH_3) for compound **25**, 299 Da

(M-H-2CH_3) for compound **26** and at 282 Da (M-H-3CH_3) for compound **29** (Zhao et al., 2020).Compound **25** showed characteristic RDA fragments at 181 Da ($MeA^{-1,3}$) and136 Da ($B^{-1,3}$), while characteristic peaks of compound 27 were at 195 Da ($2MeA^{-1,3}$) and 136 Da ($B^{-1,3}$). Moreover, the RDA fragments of compound **29** appeared at 195 Da ($2MeA^{-1,3}$) and 134 Da (Me $B^{-1,3}$). Based on the above-mentioned information and by referring to literature, compounds **25, 26** and **29** were tentatively identified as eupafolin (Huang et al., 2020), crisiliol (Moharram et al., 2012) and salvigenin (Liao et al., 2018), respectively.

4.1.3. Phenolic acids

Peaks **2, 3, 6, 8** and **9** were annotated as phenolic acids that showed a characteristic peak due to the loss of 44 Da (M-H-CO_2), though, loss of 15 Da (M-H-CH_3) was also noticed in mass spectrum of peak **6**. By referring to literature, compounds **2, 3, 6, 8** and **9** were tentatively identified as protocatechuic acid, caffeic acid, vanillic acid, coumaric acid (Kumar et al., 2017) and ferulic acid (Barros et al., 2012), respectively.

4.1.4. Iridoid glycosides

Three peaks (**5, 11** and **12)** were identified to be iridoid glycosides. All of them showed the characteristic peak (M + HCOO–H) and all of these compounds showed their major MS^2 fragment (M-H). The formate anion (M + HCOO–H) is commonly resulted from iridoid glycosides bearing an ester group or a carboxyl group at C-4 (Ren et al., 2007). Comparing to literature values, compound **5** was tentatively identified as theveside displaying characteristic peaks at 371 Da, 345 Da and 209 Da owing to loss of water, CO_2 and glucose moieties, respectively (Ren et al., 2007). Compounds **11** and **12** showed their characteristic peaks as a result of losing methoxy group (M-H-30) at 391 Da and 359 Da, respectively. Furthermore, there were fragments due to loss of glucose unit (M-H-162) from the precursor ion at 259 Da and 227 Da, respectively along with a methyl ester loss represented by the mass fragment (M - H - 60) at 361 Da and 329 Da, respectively with subsequent dehydration to afford the major product ion (M - H - 78) at 343 Da and 311 Da, respectively. Based on this information and by referring to literature, compounds **11** and **12** were tentatively identified to be lamiridoside and 8-epiloganin, respectively (Calixto et al., 2017; Czerwińska et al., 2020).

4.1.5. Phenylethanoid glycosides

Seven peaks; **4, 7, 16, 17, 18, 19** and **20** were identified as phenylethanoid glycosides. This chemical class characterized by a directly attached β-glucopyranose to hydroxyphenyl ethyl moiety. Substitution by hydroxyl derivatives of cinnamic acid (such as caffeoyl and feruloyl) usually occurs at the positions C-4 and C-6. Another sugar moiety is usually located at the C-2 or C-3 position of β-glucopyranose (Xue and Yang, 2016). Regarding compounds **16, 17, 18, 19** and **20**, the presence of two highly abundant mass fragments at 161 and 179 Da indicated the presence of caffeoyl moiety attached to the glucose unit (Li et al., 2014). Moreover, parent ions were subjected to three sequential losses of caffeoyl moiety, deoxyhexose (rhamnose) moiety (M-H-162-146) (Li et al., 2014) and glucose unit followed by dehydration to yield another daughter fragment (M-H-162-146-162-18) at 135 Da assigned for anhydrophenolethanol moiety (Attia et al., 2018). The same fragmentation pattern was also noticed for compounds **4** and **7**, however, they possessed two pentose units - rather than deoxyhexose attached to the glucose moiety, thus, two characteristic fragments appeared; the first at 315 Da (M-H-162-132-132 -162) (Li et al., 2014; Attia et al., 2018) resulting from the successive loss of caffeoyl, two pentose and glucose units. The second appeared at 135 Da (M-H-162-132-132-162-18) was owing to further loss of water moiety. Based on the mentioned information and by referring to literature, compounds **4, 7, 16, 17, 18, 19** and were tentatively identified as fucatoside B (Juliao et al., 2009), fucatoside C (Juliao et al., 2009), arenarioside (Gong et al., 2020), verbascoside (Attia et al., 2018), cis-verbascoside (Ashour, 2021), isoverbascoside (Ashour, 2021) and Parvifloroside A (Juliao et al., 2009), respectively.

4.1.6. Lignan glycosides

One peak was identified to be a lignan glycoside (Peaks **15**). It showed two characteristic peaks at 423 Da (M-H- 162) and 570 Da (M-H-15) due to loss of glucose and methyl group, respectively. This compound was identified as radulignan (Filho et al., 2009).

4.1.7. Miscellaneous compounds

Compound **10** presented a deprotonated ion peak at 45 Da (M-H-galactose) and it was tentatively identified as ethyl-β-D-galactoside (Misra et al., 2007). The tentatively identified linaloic acid hexoside (menthiafolic acid hexoside, peak **13**) was successively dehydrated to afford fragments at 327 Da (M-H-H_2O) and 309 Da (M-H-2H_2O) provided additional fragments at 183 Da (M-H-162) due to hexose loss (Goodger and Woodrow, 2013). Compound **27** was recognized as a naphthoquinone derivative and this was deduced from its characteristic fragments at305 Da (M-H-CO), 277 Da (M-H–CO–CO) in addition to a fragment due to the loss of methyl group (M-H-CH_3) (Elwoo et al., 1970) and by referring to literature it was tentatively identified as lantalucratin F (Hayash et al., 2004). Finally, compound **28** was identified as furanonaphthoquinone derivative, representing characteristic fragments (M-H-CO) and (M-H–CO–CO) (Diaz and Medina, 1996) and by referring to literature it was identified as 5-hydroxynaphtho[2,3-b]furan-4, 9-dione (Abeygunawardena et al., 1991).

4.2. Investigation of the inter-cultivar effect on the metabolic profile using multivariate statistical analysis of the UPLC-MS/MS data

4.2.1. Unsupervised pattern recognition

The UPLC-MS/MS data matrix was subjected to the unsupervised pattern recognition, principal component analysis (PCA) (Fig. 2A) in order to explore the clustering pattern of different *Lantana* cultivars extracts based on their chemical profiles. The first two principal components (PC1, PC2) represent 55% of total variation within all samples. The model was valid as it showed R2X (cum) value of 0.98 indicating the goodness of fit of the model. Its predictive power was significantly high as indicated by the Q2 (cum) value of 0.95.

The loading plot (Fig. 2B) showed the distribution of chemical constituents among different hydroalcoholic extracts of *L. camara* cultivars. Therefore, it can identify the chemical markers that are responsible for samples segregation.

4.3. Cytotoxicity and anti-COVID activity of the tested extracts

4.3.1. Assessment of the cytotoxicity of the tested extracts on Vero E6 cells

MTT assay was used to assess the effect of the tested extracts on the viability of Vero E6 cells (Green monkeys kidney cells) (Table 2).

4.3.2. Anti-COVID-19 activity using plaque reduction assay

The antiviral activity of the tested extracts against (COVID-19) beta (B.1.1.3.) strains was evaluated using plaque reduction assay. IC_{50} values were determined using Graphpad Instat software (GraphPad Software Inc, California) by plotting % reduction against different concentrations of each tested extract (Table 2). In order to ensure the safety and efficacy of the tested extracts, the selectivity indices that measures the window between the cytotoxicity and antiviral activity (Indrayanto et al., 2021) were calculated based on CC_{50} values obtained from MTT test and IC_{50} values of plaque reduction assay. The higher the selectivity index, the safer and the more effective the drug is (Indrayanto et al., 2021).

4.3.3. Effects of the tested extracts on expression of SARS-CoV-2 RdRp and E genes

The promising safety and antiviral activity of the aforementioned

extracts have triggered the need to deeply understand the possible mechanisms of their anti-COVID-19 activity. This was achieved by estimating the transcript levels of RdRp and E genes using a TaqMan Real-time RT-PCR assay. Although coronavirus has many viral proteins, many studies showed and proved that RdRp is the most relevant viral target to identify specific anti-COVID-19 agents, as it is considered as a vital enzyme for the life cycle of RNA viruses because it is responsible for viral RNA replication in host cells which lack an enzymatic counterpart (Zhao et al., 2021). In fact, viral polymerases inhibitors represent the cornerstone of antiviral therapeutics; indeed, most of the approved drugs for the treatment of viral infections, including HIV and HCV, belong to this class (Cannalire et al., 2020; Cui et al., 2020; Elfiky, 2020; Wu et al., 2020). On the other hand, E gene encodes a small and significant structural protein for coronaviruses which in turn contributes to many vital processes of coronaviruses, such as assembly, budding, and envelope formation making it an important target for anti-COVID-19 drugs (Sun et al., 2020). Four levels of extracts' safe concentrations (30, 15, 12.5, 6.25 μg/mL) were plotted against the % down regulation of RdRp and E genes (Fig. 3).

4.4. Determination of the anti-COVID-19 biomarkers using supervised pattern recognition analysis

In order to investigate the clustering of the tested extracts based on their anti-COVID-19 activity in addition to determination of the biomarkers that are responsible for such activity, UPLC-MS/MS data matrix (X-variables) and IC_{50} values obtained from plaque reduction assay (Y-variables) were imported to Orthogonal Projection to Latent Structure (OPLS) as one of supervised pattern recognition models. The OPLS model showed goodness of fit (R^2) value of 0.99 and good predictive power (Q2) value of 0.97 indicating the validity of the model (Fig. 4).

Coefficient plot (Fig. 5) was constructed to determine the metabolites which had positive contribution to the anti-COVID-19 activity of the studied extracts. It is interesting to note that twelve biomarkers (positive contributors) associated with COVID-19 inhibitory activity were determined. These biomarkers were found in high concentration in the most active extracts as following: camaric acid, lantanilic acid, lantiursolic acid, luteolin-7,4'-O diglucoside, lantabetulic acid, camarolic acid, icterogenin, lantaoic acid, camaranoic acid, lantacin and lantic acid were present in the highest concentration in *L. camara* cv. Chelsea gem leaves extract. Meanwhile, ferulic acid was detected in a high concentration in *L. camara* cv. Spreading sunset flower extract, while isoverbascoside scored the highest concentration in the leaves extract of *L. camara* cv. Drap d'or. This could explain the remarkable contribution of these biomarkers to the stunning anti-COVID-19 potentials of such extracts that ultimately discriminated them from cluster B extracts (Fig. 4). By referring to literature, the identified biomarkers were found to have antiviral activity. Ferulic acid exhibited antiviral activity against plant viruses and H1N1 virus (Hariono et al., 2016; Wang et al., 2017). Many studies showed that ursane and oleane type triterpenes possessed antiviral activity mainly against respiratory viruses (Chen et al., 2020; Jesus et al., 2015; Khwaza et al., 2018; Pawełczyk and Zaprutko, 2020; Tohmé et al., 2019). Moreover, a previous study revealed that isoverbascoside possessed a high binding affinity to SARS-CoV-2 (Banerjee et al., 2021a). Furthermore, luteolin was proved to have antiviral activity against different viral strains (Ninfali et al., 2020).

4.5. Molecular docking studies on the biomarkers

RdRp (NSP12) plays its crucial role in the viral transcription cycle with the help of cofactors NSP7 and NSP8 that are present in its crystal structure. Its active site is tunnel shaped cavity located between the NiRAN (nucleotidyltransferase) domain β-hairpin constituting 398–919 amino acid residues, in which the catalytic residues were localized (Vardhan and Sahoo, 2020a). RdRp hydrophobic cavities at active N and C-terminals are involved in catalysis of RNA polymerization (Vardhan and Sahoo, 2020b). The catalytic active site of the RdRp consists of seven conserved motifs (A to G); The RNA template is expected to enter the active site composed of motifs A and C through a groove clamped by motifs F and G. The NTP (nucleotide triphosphate) entry channel is formed by a set of hydrophilic residues, including LYS545, ARG553, ARG555 and ASN691 in motif F that are predicted to play roles in drug interactions (Abd El-Aziz et al., 2021). Strong electrostatic surfaces are observed via divalent cationic residues 611–626, especially the residue ASP618. Some others are also located between residues 753–769 (Vardhan and Sahoo, 2020a), hence, these residues Asp618, Ser759, Asp760, Asp761, Asp623, Arg555, Arg553, Lys545, Val557, Ser682, Asn691 and Thr680 were used for receptor grid generation and screening of compounds.

Since RdRp was previously observed as the main target of action for the tested extracts' anti-COVID activity, hence; the predetermined biomarkers were docked into its active site in order to investigate the possible interaction patterns and afford deep understanding to the molecular mechanisms of action of these molecules. For the screening purposes, remdesivir was used as an example of FDA approved drugs for comparative analysis (Abd El-Aziz et al., 2021).

The molecular interaction analysis of these top hit compounds with SARS-CoV-2 RdRp revealed that they were involved in interactions with most of the aforementioned amino acid residues confirming that they were successfully docked into the RdRp binding site (Aouidate et al., 2021).

The docked pose of remdesivir against RdRp was represented in Figure (6). Herein, it was found that it fitted well into the active site via forming hydrogen bonds with Asp761, Tyr619, Arg553, Cys622 as well as negatively charged interactions with Asp623, Asp618, Asp760 and Asp761. Positively charged interactions with Lys621, Arg624, Arg553, Arg555 and Lys545 alongside, hydrophobic interactions with Trp617, Glu813, Leu758, Cys622, Tyr619, Tyr455 and Val557 were also observed. Remdesivir also bound to the core protein through polar interactions with the amino acid residues: Ser759, Ser814, Thr556, Ser682; one salt bridge and another pi-pi interaction with Arg553. These interactions were in close agreement to those reported in literature which proved their important role in enzyme catalysis (Tiwari, 2021).

Comparing the 2D interaction diagrams of the top hit compounds: isoverbascoside, luteolin-7, 4'-O -diglucoside, camarolic acid and lantoic acid (Figs. 7 and 8) to that of remdesivir demonstrated common positive charged interactions with the amino acids Arg553 and Arg555 that constitute part of this polymerase NTP channel structure. That signified their crucial role in the enzyme inhibition via preventing the entry of adenosine triphosphate (ATP) and divalent cations into the central active site cavity, thus attenuating RNA replication (Abd El-Aziz et al., 2021). However, isoverbascoside was involved in ten H-bonds (Arg624, Thr556, Tyr619, Asp618, Asp760, Lys621 and Ser795); luteolin-7, 4'-O-diglucoside was involved in seven H-bonds (Asp760, Asp761, Ser682, Thr556, Lys621, Asp619); camarolic acid was incorporated in six H-bonds (Arg55, Arg553, Lys545, Asp452 and Thr556) and lantoic acid was engaged in four hydrogen bonds (Asn691, Arg555, Arg553 and Lys551) compared to remdesivir (exhibiting only three bonds with Asp761, Tyr619 and Arg553). As a result, better interaction (as expressed by their docking GScores) and stronger inhibition of the SARS-CoV-2 RdRp was achieved.

In addition to the highest number of hydrogen bonding interactions displayed by isoverbascoside, it was engaged in more negative and positive charged interactions with the key amino acid residues (Fig. 7), leading to formation of the most stable complex within the active site of the RdRp protein, hence; the highest Gscore value.

From Figs. 7 and 8, it has been postulated that luteolin- 7, 4'-O-diglucoside had the tendency to form a more conformationally fitting complex than camarolic and lantoic acids through the formation of higher number of hydrogen bonds, hydrophobic and negatively charged interactions, thus might contribute significantly to its higher *in-silico* COVID-19 inhibitory activity.

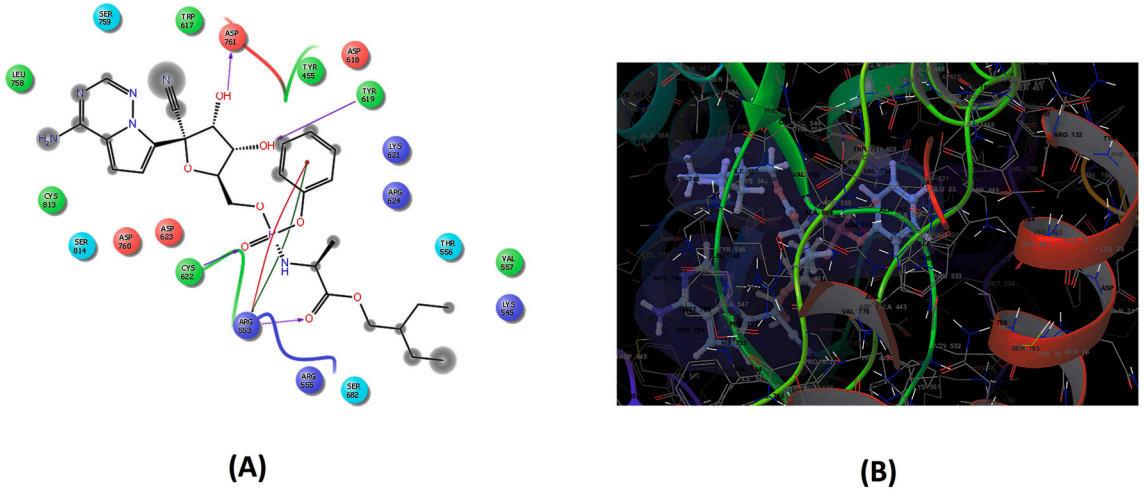

Fig. 6. 2D (A) and 3D (B) ligand interaction diagrams for docking poses of the known FDA approved anti-viral remdesivir in the active site of SARS-CoV-2 RdRp crystalline structure (PBD ID 6M71).

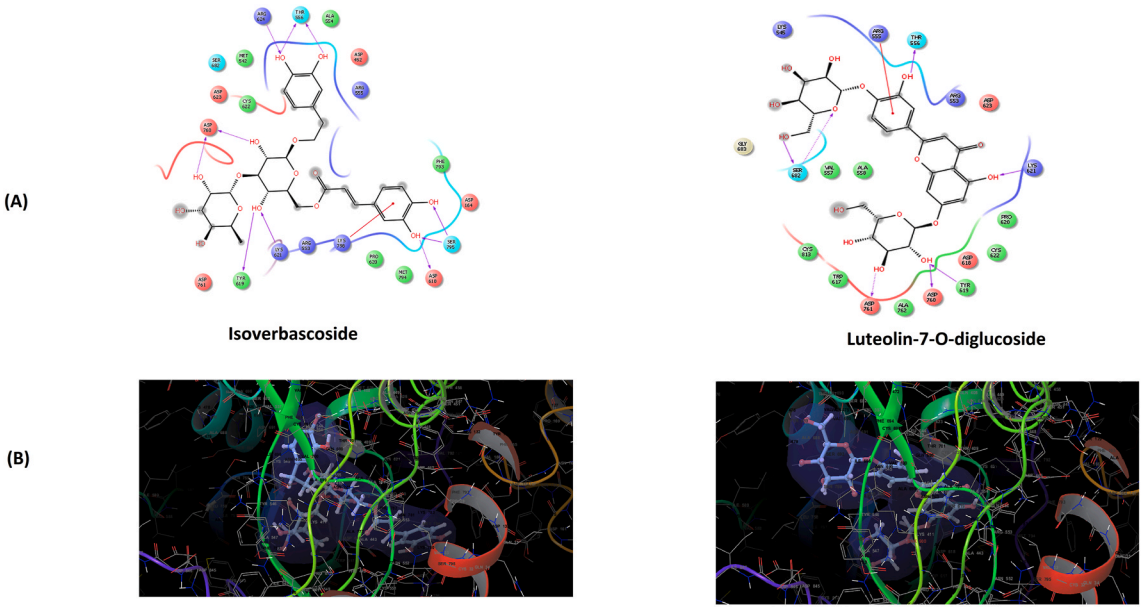

Fig. 7. 2D (A) and 3D (B) ligand interaction diagrams for docking poses of isoverbascoside and luteolin −7, 4'-O -diglucoside in the active site of SARS-CoV-2 RdRp crystalline structure (PBD ID 6M71).

Camarolic and lantoic acids are considered as examples of oleanane and ursane type pentacyclic triterpenes, respectively, that share many structural similarities including a C-28 carboxylic acid and two hydroxyls at C-33 and C-22. However, it seemed that substituents at the hydroxy group of C-22 such as 3-hydroxy-2-methylene butanoyl moieties were notably integrated in favourable interactions with the enzyme. For instance, both compounds shared the same number of H-bonds via their carboxylic group at C-28, however camarolic acid was observed to engage in extra four H-bonds with the surface accessible residues Arg553, Asp452 and Thr556, unlike lantoic acid, which lacked the 3-hydroxy-2-methylene butanoyl moiety at C-22. This in turn limited the number of hydrogen bonds formed to only one with Lys551(Fig. 8).

Recent studies have reported the *in-vitro* inhibitory activity of isoverbascoside to SARS-CoV-2 main protease (Banerjee et al., 2021a) in addition to its antiviral activity against respiratory syncytial virus (Kernan et al., 1998). Literature lacks accurate information regarding the efficacy of luteolin-7,4'-O-diglucoside and lantoic acid as anti-viral drugs, while promising anti-viral activity of camarolic acid as a pentacyclic oleanolic acid triterpene was previously noted (Banik and Pandey, 2008). As far as we know, no inhibitory activity to SARS-CoV-2 RdRp was reported for such compounds. This triggers the critical need for their targeted isolation coupled with extensive *in-vitro* and *in-vivo* studies to afford deep explanation and verification of their promising *in-silico* activities. These comprehensive studies might be incorporated in presenting new COVID-19 inhibitors which have not previously reported for this activity.

5. Conclusion

In conclusion, extracts of four *L. camara* cultivars were recognized as rich sources of health promoting phytoconstituents for the human being especially in attenuating COVID-19 virus as a newly reported activity that was not previously reported despite the plant's historical role in alleviating respiratory ailments. The combination of a multiplatform metabolite profiling using UPLC-MS/MS and chemometrics is a promising approach to afford deep understanding to the chemical

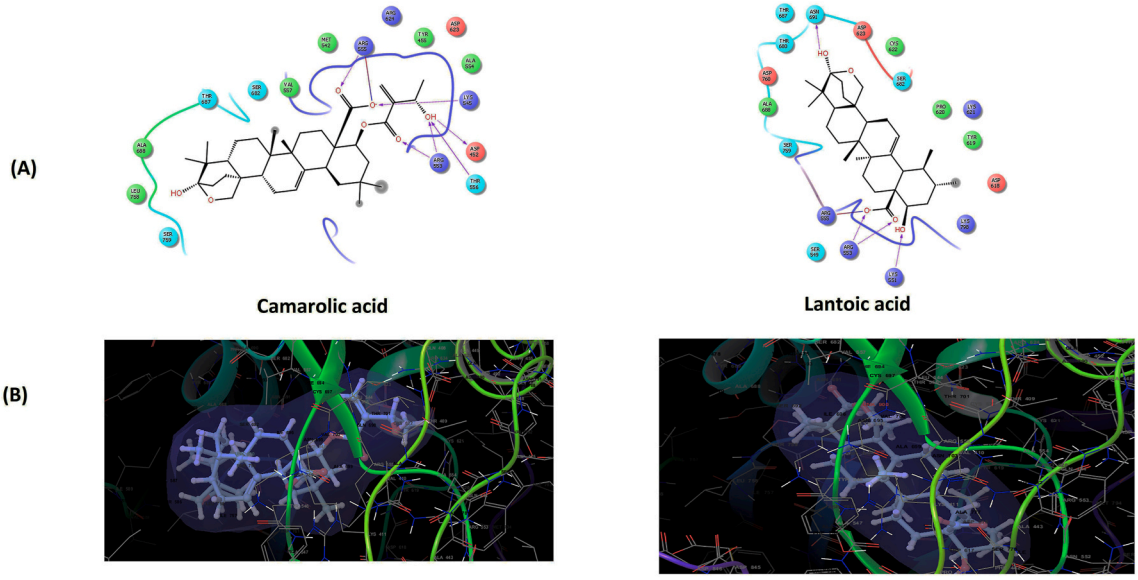

Fig. 8. 2D (A) and 3D (B) ligand interaction diagrams for docking poses of camarolic acid and lantoic acid in the active site of SARS-CoV-2 RdRp crystalline structure (PBD ID 6M71).

composition differences among the cultivars extracts and correlate them to COVID-19 inhibitory activities allowing to pinpoint possible candidate metabolites responsible for the biological activity of the extracts. Since molecular docking studies confirmed the promising activities of isoverbascoside, luteolin-7, 4'-O-diglucoside, camarolic and lantoic acids, our future perspective will focus on isolation of these biomarkers, and subjecting them to extensive *in-vitro, in-vivo* and clinical studies aiming to provide verification to their promising *in-silico* activities.

Authors' contribution

Reham S. Darwish**:** Conceptualization, Methodology, Data curation, Writing- Original draft preparation, Supervision, Validation, Writing-Reviewing and Editing.

Alaa A. El Banna: Methodology, Writing, Original draft preparation, Visualization Reviewing and Editing.

Doaa Ghareeb: Methodology, Data curation, Writing- Original draft preparation.

Mostafa F. M. Hoseny: Methodology, Data curation, Writing- Original draft preparation.

Mohamed G. S. Khamis: Methodology, Data curation, Writing-Original draft preparation.

Hend M. Dawood: Conceptualization, Methodology, Data curation, Writing- Original draft preparation, Supervision, Validation, Writing-Reviewing and Editing.

Declaration of competing interest

The authors have declared no conflict of interest.

Appendix A. Supplementary data

Supplementary data to this article can be found online at https://doi.org/10.1016/j.jep.2022.115038.

References

Abd El-Aziz, N.M., Eldin Awad, O.M., Shehata, M.G., El-Sohaimy, S.A., 2021. Inhibition of the SARS-CoV-2 RNA-Dependent RNA polymerase by natural bioactive compounds: molecular docking analysis. Egypt. J. Chem. 64, 1989. https://doi.org/10.21608/EJCHEM.2021.45739.2947, 2001.

Abeygunawardena, G., Kumar, V., Marshall, D.S., Thomson, R.H., Wickramaratne, D.B. M., 1991. Furanonaphthoquinones from two lantana species. Phytochemistry 30, 941–945.

Alam, S., Sarker, M.M.R., Afrin, S., Richi, F.T., Zhao, C., Zhou, J.R., Mohamed, I.N., 2021. Traditional herbal medicines, bioactive metabolites, and plant products against COVID-19: update on clinical trials and mechanism of actions. Front. Pharmacol. 12, 1–20. https://doi.org/10.3389/fphar.2021.671498.

Alberti-Dér, Á., 2013. LC-ESI-MS/MS Methods in Profiling of Flavonoid Glycosides and Phenolic Acids in Traditional Medicinal Plants: Sempervivum Tectorum L. And Corylus Avellana L.

Aouidate, A., Ghaleb, A., Chtita, S., Aarjane, M., Ousaa, A., Maghat, H., Sbai, A., Choukrad, M., Bouachrine, M., Lakhlifi, T., 2021. Identification of a novel dual-target scaffold for 3CLpro and RdRp proteins of SARS-CoV-2 using 3D-similarity search, molecular docking, molecular dynamics and ADMET evaluation. J. Biomol. Struct. Dyn. 39, 4522–4535. https://doi.org/10.1080/07391102.2020.1779130.

Ashour, M.A., 2021. Isolation, HPLC/UV Characterization and Antioxidant Activity of Phenylethanoids from Blepharis Edulis (Forssk.) Pers. Growing in Egypt, vol. 50. Bulletin of Faculty of Pharmacy, Cairo University une, pp. 67–72.

Attia, Y.M., El-Kersh, D.M., Wagdy, H.A., Elmazar, M.M., 2018. Verbascoside: identification, quantification, and potential sensitization of colorectal cancer cells to 5-FU by targeting PI3K/AKT pathway. Sci. Rep. 8, 1–12.

Ayatollahi, A., Ghanadian, M., Afsharypour, S., Abdella, O.M., Mirzai, M., Askari, G., 2011. Pentacyclic triterpenes in Euphorbia microsciadia with their T-cell proliferation activity. Iran. J. Pharm. Res. (IJPR) 10, 287–294.

Banerjee, R., Perera, L., Tillekeratne, L.M.V., 2021a. Potential SARS-CoV-2 main protease inhibitors. Drug Discov. Today 26, 804–816. https://doi.org/10.1016/j.drudis.2020.12.005.

Banerjee, S., Kar, A., Mukherjee, P.K., Haldar, P.K., Sharma, N., Katiyar, C.K., 2021b. Immunoprotective potential of Ayurvedic herb Kalmegh (Andrographis paniculata) against respiratory viral infections – LC–MS/MS and network pharmacology analysis. Phytochem. Anal. 32, 629–639. https://doi.org/10.1002/pca.3011.

Banik, R.M., Pandey, D.K., 2008. Optimizing conditions for oleanolic acid extraction from Lantana camara roots using response surface methodology. Ind. Crop. Prod. 27, 241–248. https://doi.org/10.1016/j.indcrop.2007.09.004.

Barros, L., Dunas, M., Dias, M.I., Santos-Buelga, C., Ferreira, I.C.F.R., 2012. Phenolic profiles of in vivo and in vitro grown Coriandrum sativum L. Food Chem. 132, 841–848.

Begum, S., Ayub, A., Zehra, S.Q., Siddiqui, B.S., Choudhary, M.I., Samreen, 2014. Leishmanicidal triterpenes from lantana camara. Chem. Biodivers. 11, 709–718.

Begum, S., Zehra, S.Q., Siddiqui, B.S., Fayyaz, S., Ramzan, M., 2008. Pentacyclic triterpenoids from the aerial parts of lantana camara and TheirNematicidal activity. Chem. Biodivers. 5, 1856–1866.

Beigel, J.H., Tomashek, K.M., Dodd, L.E., Mehta, A.K., Zingman, B.S., Kalil, A.C., Hohmann, E., Chu, H.Y., Luetkemeyer, A., Kline, S., Lopez de Castilla, D., Finberg, R. W., Dierberg, K., Tapson, V., Hsieh, L., Patterson, T.F., Paredes, R., Sweeney, D.A., Short, W.R., Touloumi, G., Lye, D.C., Ohmagari, N., Oh, M., Ruiz-Palacios, G.M., Benfield, T., Fätkenheuer, G., Kortepeter, M.G., Atmar, R.L., Creech, C.B., Lundgren, J., Babiker, A.G., Pett, S., Neaton, J.D., Burgess, T.H., Bonnett, T., Green, M., Makowski, M., Osinusi, A., Nayak, S., Lane, H.C., 2020. Remdesivir for the treatment of covid-19 — final report. N. Engl. J. Med. 383, 1813–1826. https://doi.org/10.1056/NEJMOA2007764/SUPPL_FILE/NEJMOA2007764_DATA-SHARING.PDF.

Borges, D.G.L., Echeverria, J.T., de Oliveira, T.L., Heckler, R.P., de Freitas, M.G., Damasceno-Junior, G.A., Carollo, C.A., Borges, F. de A., 2019. Discovery of potential ovicidal natural products using metabolomics. PLoS One 14, e0211237.
Brito, A., Ramirez, J.E., Areche, C., Sepúlveda, B., Simirgiotis, M.J., 2014. HPLC-UV-MS profiles of phenolic compounds and antioxidant activity of fruits from three citrus species consumed in northern Chile. Molecules 19, 17400–17421.
Calixto, N.O., Cordeiro, M.S., Giorno, T.B.S., Oliveira, G.G., Lopes, N.P., Fernandes, P.D., Pinto, A.C., Rezende, C.M., 2017. Chemical constituents of Psychotria nemorosa gardner and antinociceptive activity. J. Braz. Chem. Soc. 28, 707–723. https://doi.org/10.21577/0103-5053.20160219.
Caly, L., Druce, J.D., Catton, M.G., Jans, D.A., Wagstaff, K.M., 2020. The FDA-approved drug ivermectin inhibits the replication of SARS-CoV-2 in vitro. Antivir. Res. 178, 104787. https://doi.org/10.1016/J.ANTIVIRAL.2020.104787.
Cannalire, R., Cerchia, C., Beccari, A.R., di Leva, F.S., Summa, V., 2020. Targeting SARS-CoV-2 proteases and polymerase for COVID-19 treatment: state of the art and future opportunities. J. Med. Chem. 65 (4), 2716–2746. https://doi.org/10.1021/ACS.JMEDCHEM.0C01140/SUPPL_FILE/JM0C01140_SI_001.PDF.
Chen, Q., Zhang, Y., Zhang, W., Chen, Z., 2010. Identification and quantification of oleanolic acid and ursolic acid in Chinese herbs by liquid chromatography–ion trap mass spectrometry. Biomed. Chromatogr. 25, 1381–1388.
Chen, Y., Li, H., Wu, L., Wu, L., Zhang, M., Gao, Y., Wang, H., Wang, H., Xu, D., Xu, D., Chen, W., Song, G., Song, G., Chen, J., Chen, J., 2020. Ursolic acid derivatives are potent inhibitors against porcine reproductive and respiratory syndrome virus. RSC Adv. 10, 22783–22796. https://doi.org/10.1039/d0ra04070c.
Civitelli, L., Panella, S., Marcocci, M.E., de Petris, A., Garzoli, S., Pepi, F., Vavala, E., Ragno, R., Nencioni, L., Palamara, A.T., Angiolella, L., 2014. In vitro inhibition of herpes simplex virus type 1 replication by Mentha suaveolens essential oil and its main component piperitenone oxide. Phytomedicine 21, 857–865. https://doi.org/10.1016/J.PHYMED.2014.01.013.
Corman, V.M., Landt, O., Kaiser, M., Molenkamp, R., Meijer, A., Chu, D.K.W., Bleicker, T., Brünink, S., Schneider, J., Schmidt, M.L., Mulders, D.G.J.C., Haagmans, B.L., van der Veer, B., van den Brink, S., Wijsman, L., Goderski, G., Romette, J.L., Ellis, J., Zambon, M., Peiris, M., Goossens, H., Reusken, C., Koopmans, M.P.G., Drosten, C., 2020. Detection of 2019 novel coronavirus (2019-nCoV) by real-time RT-PCR. Euro Surveill. 25, 2000045. https://doi.org/10.2807/1560-7917.ES.2020.25.3.2000045/CITE/PLAINTEXT.
Cui, W., Yang, K., Yang, H., 2020. Recent progress in the drug development targeting SARS-CoV-2 main protease as treatment for COVID-19. Front. Mol. Biosci. 7, 398. https://doi.org/10.3389/FMOLB.2020.616341/BIBTEX.
Czerwińska, M.E., Kalinowska, E., Popowski, D., Bazylko, A., 2020. Lamalbid, chlorogenic acid, and verbascoside as tools for standardization of lamium album flowers—development and validation of HPLC–DAD method. Molecules 25. https://doi.org/10.3390/molecules25071721.
Darwish, R.S., Hammoda, H.M., Ghareeb, D.A., Abdelhamid, A.S.A., El Naggar, E.B., Harraz, F.M., Shawky, E., 2020. Efficacy-directed discrimination of the essential oils of three Juniperus species based on their in-vitro antimicrobial and anti-inflammatory activities. Ethnopharmacology 259, 1–12.
DeDiego, M.L., Nieto-Torres, J.L., Jiménez-Guardeño, J.M., Regla-Nava, J.A., Álvarez, E., Oliveros, J.C., Zhao, J., Fett, C., Perlman, S., Enjuanes, L., 2011. Severe acute respiratory syndrome coronavirus envelope protein regulates cell stress response and apoptosis. PLoS Pathog. 7, e1002315.
Dettmer, K., Aronov, P.A., Hammock, B.D., 2007. Mass spectrometry-based metabolomics. Mass Spectrom. Rev. 26, 51–78. https://doi.org/10.1002/mas.20108.
Diaz, F., Medina, J.D., 1996. Furanonaphthoquinones from Tabebuia ochracea ssp. neochrysanta. J. Nat. Prod. 1 59, 423–424.
El Gendy, S.N., 2019. Phytochemical and biological study of lantana camara L. (Family verbenaceae) growing in Egypt. CU Theses.
Elfiky, A.A., 2020. SARS-CoV-2 RNA dependent RNA polymerase (RdRp) targeting: an in silico perspective. J. Biomol. Struct. Dynam. 39, 3204–3212. https://doi.org/10.1080/07391102.2020.1761882.
El-Hoshoudy, A.N., 2020. Investigating the potential antiviral activity drugs against SARS-CoV-2 by molecular docking simulation. J. Mol. Liq. 318, 113968.
Elwoo, T., Dudleyj, K., Tesarek, J.M., Rogerson, P.F., Bursey, M., 1970. The mass spectra OF some naphthoquinones. LAPACHOL, ISOLAPACHOL and related compounds. Org. Mass Spectrom. 3, 841–861.
Fabre, N., Rustan, I., Hoffmann, E.d., Quetin-Leclercq, J., 2001. Determination of flavone, flavonol, and flavanone aglycones by negative ion liquid chromatography electrospray ion trap mass spectrometry. American Society for Mass Spectrometry 12, 707–715.
Filho, J.G.S., Nimmo, S.L., Xavier, H.S., Barbosa-Filho, J.M., Cichewicz, R.H., 2009. Phenylethanoid and lignan glycosides from polar extracts of Lantana, a genus of verbenaceous plants widely used in traditional herbal therapies. J. Nat. Prod. 72, 1344–1347.
Fuzimoto, A.D., Isidoro, C., 2020. The antiviral and coronavirus-host protein pathways inhibiting properties of herbs and natural compounds - additional weapons in the fight against the COVID-19 pandemic? Journal of Traditional and Complementary Medicine 10, 405–419. https://doi.org/10.1016/j.jtcme.2020.05.003.
Ghallab, D.S., Mohyeldin, M.M., Shawky, E., Metwally, A.M., Ibrahim, R. said, 2020. Chemical profiling of Egyptian propolis and determination of its xanthine oxidase inhibitory properties using UPLC–MS/MS and chemometrics. LWT- Food Science and Technology 136, 1–16.
Gong, X., Wang, J., Zhang, M., Wang, P., Wang, C., Shi, R., Zang, E., Zhang, M., Zhang, C., Li, M., 2020. Bioactivity, compounds isolated, chemical qualitative, and quantitative analysis of cymbaria daurica extracts. Front. Pharmacol. 11, 1–12.
Goodger, J.Q.D., Woodrow, I.E., 2013. Chapter 12 - oleuropeic and menthiafolic acid glucose esters from plants: shared structural relationships and biological activities. In: Studies in Natural Products Chemistry. Elsevier B.V., pp. 427–452
Hariono, M., Abdullah, N., Damodaran, K.V., Kamarulzaman, E.E., Mohamed, N., Hassan, S.S., Shamsuddin, S., Wahab, H.A., 2016. Potential new H1N1 neuraminidase inhibitors from ferulic acid and vanillin: molecular modelling, synthesis and in vitro assay. Sci. Rep. 6, 1–10. https://doi.org/10.1038/srep38692.
Hasan, R., 2017. Antiviral Activity of Leaves extract of lantana camara against the replication of virus A/Puerto Rico/8/34(PR8). Iraqi J. Sci. 10, 1–8.
Hayash, K., Chang, F., Nakanishi, Y., Bastow, K.F., Cragg, G., McPhail, A.T., Nozaki, H., Lee, K., 2004. Antitumor agents. 233.1 lantalucratins A−F, new cytotoxic naphthoquinones from lantana involucrata. J. Nat. Prod. 67, 990–993.
Huang, G., Liang, J., Chen, X., Lin, J., Wei, J., Huang, D., Zhou, Y., Sun, Z., Zhao, L., 2020. Isolation and identification of chemical constituents from zhideke granules by ultra-performance liquid chromatography coupled with mass spectrometry. J. Anal. Methods Chem. 1–16, 2020.
Huang, S.-T., Chen, Y., Chang, W.-C., Chen, H.-F., Lai, H.-C., Lin, Y.-C., Wang, W.-J., Wang, Y.-C., Yang, C.-S., Wang, S.-C., 2021. Scutellaria barbata D. Don inhibits the main proteases (mpro and TMPRSS2) of severe acute respiratory syndrome coronavirus 2 (SARS-CoV-2) infection. Viruses 13, 826.
Indrayanto, G., Putra, G.S., Suhud, F., 2021. Validation of in-vitro bioassay methods: application in herbal drug research. Profiles Drug Subst. Excipients Relat. Methodol. 46, 273–307.
Jesus, J.A., Lago, J.H.G., Laurenti, M.D., Yamamoto, E.S., Passero, L.F.D., 2015. Antimicrobial activity of oleanolic and ursolic acids: an update. Evid. base Compl. Alternative Med. 1–14, 2015.
Juliao, L.d., Piccinelli, A.L., Marzocco, S., Leitao, S.G., Lotti, C., Autore, G., Rastrell, L., 2009. Phenylethanoid glycosides from lantana fucata with in vitro anti-inflammatory activity. J. Nat. Prod. 72, 1424–1428.
Kachlicki, P., Piasecka, A., Stobiecki, M., Marczak, Ł., 2016. Structural characterization of flavonoid glycoconjugates and their derivatives with mass spectrometric techniques. Molecules 21, 1–21.
Kalita, S., Kumar, G., Karthik, L., Rao, K.V.B., 2012. A review on medicinal properties of lantana camara linn. Res. J. Pharm. Technol. 5, 711–715.
Kanagavalli, R., kumar, M., Vijayan, P., kumar, M., Kavitha, K., Singh, S.D.J., 2011. In-vitro antiviral screening of Lantana camara stem extract. Res. J. Pharmaceut. Biol. Chem. Sci. 2, 940–946.
Kernan, M.R., Amarquaye, A., Chen, J.L., Chan, J., Sesin, D.F., Parkinson, N., Ye, Z., Barrett, M., Bales, C., Stoddart, C.A., Sloan, B., Blanc, P., Limbach, C., Mrisho, S., Rozhon, E.J., 1998. Antiviral phenylpropanoid glycosides from the medicinal plant Markhamia lutea. J. Nat. Prod. 61, 564–570. https://doi.org/10.1021/np9703914.
Khwaza, V., Oyedeji, O.O., Aderibigbe, B.A., 2018. Antiviral activities of oleanolic acid and its analogues. Molecules 23. https://doi.org/10.3390/molecules23092300.
Kikuchi, T., Tanaka, A., Uriuda, M., Yamada, T., Tanaka, R., 2016. Three novel triterpenoids from Taraxacum officinale roots. Molecules 21, 1–11.
Kumar, S., Singh, A., Kumar, B., 2017. Identification and characterization of phenolics and terpenoids from ethanolic extracts of Phyllanthus species by HPLC-ESI-QTOF-MS/MS. J. Pharm. Anal. 7, 214–222. https://doi.org/10.1016/j.jpha.2017.01.005.
Li, C., Liu, Y., Abdulla, R., Aisab, H.A., Suo, Y., 2014. Characterization and identification of chemical components in Neopicrorhiza scrphulariiflora roots by liquid chromatography-electrospray ionization quadrupole time-of-flight tandem mass spectrometry. Anal. Methods 6, 3634–3643.
Li, Z.-H., Guo, H., Xu, W.-B., Ge, J., Li, X., Alimu, M., He, D.-J., 2016. Rapid identification of flavonoid constituents directly from PTP1B inhibitive extract of raspberry (rubus idaeus L.) leaves by HPLC–ESI–QTOF–MS-MS. J. Chromatogr. Sci. 54, 805–810.
Liao, M., Cheng, X., Zhang, X., Diao, X., Liang, C., Zhang, L., 2018. Qualitative and quantitative analyses of active constituents in trollius ledebourii. J. Chromatogr. Sci. 56, 619–635.
Misra, N., Sharma, M., Raj, K., Dangi, A., Srivastava, S., Misra-Bhattacharya, S., 2007. Chemical constituents and antifilarial activity of Lantana camara against human lymphatic filariid Brugia malayi and rodent filariid Acanthocheilonema viteae maintained in rodent hosts. Parasitol. Res. 100, 439–448.
Moharram, F.A., Marzouk, M.S., El-Shenawyf, S.M., Gaarac, A.H., El Kady, W.M., 2012. Polyphenolic profile and biological activity of Salvia splendens leaves. Roy. Pharm. Soc. J. Phar. Pharmacol. 64, 1678–1687.
Mohideen, A.K.S., 2021. Molecular docking analysis of phytochemical thymoquinone as a therapeutic agent on SARS-Cov-2 envelope protein. Biointerface . Res. Appl. Chem. 11, 8389–8401.
Mosmann, T., 1983. Rapid colorimetric assay for cellular growth and survival: application to proliferation and cytotoxicity assays. J. Immunol. Methods 65, 55–63.
Narkhede, R.R., Cheke, R.S., Ambhore, J.P., Shinde, S.D., 2020. The molecular docking study of potential drug candidates showing anti-COVID-19 activity by exploring of therapeutic targets of SARS-CoV-2. Eur. J. Med. Oncol. 4, 185–195.
Negi, G.C.S., Sharma, S., Vishvakarma, S.C.R., Samant, S.S., Maikhuri, R.K., Prasad, R.C., Palni, L.M.S., 2019. Ecology and use of lantana camara in India. Bot. Rev. 85, 109–130. https://doi.org/10.1007/s12229-019-09209-8.
Ninfali, P., Antonelli, A., Magnani, M., Scarpa, E.S., 2020. Antiviral properties of flavonoids and delivery strategies. Nutrients 12, 1–19. https://doi.org/10.3390/nu12092534.
Pawełczyk, A., Zaprutko, L., 2020. Anti-COVID drugs: repurposing existing drugs or search for new complex entities, strategies and perspectives. Future Med. Chem. 12, 1743–1757. https://doi.org/10.4155/fmc-2020-0204.
Payne, S., 2017. Family Coronaviridae. Viruses 149. https://doi.org/10.1016/B978-0-12-803109-4.00017-9.
Peele, K.A., Potla Durthi, C., Srihansa, T., Krupanidhi, S., Ayyagari, V.S., Babu, D.J., Indira, M., Reddy, A.R., Venkateswarulu, T.C., 2020. Molecular docking and

dynamic simulations for antiviral compounds against SARS-CoV-2: a computational study. Informat. Med. Unlocked 19, 100345. https://doi.org/10.1016/j.imu.2020.100345.

Puig-Castellví, F., Cardona, L., Jouan-Rimbaud Bouveresse, D., Cordella, C.B.Y., Mazéas, L., Rutledge, D.N., Chapleur, O., 2020. Assessment of substrate biodegradability improvement in anaerobic Co-digestion using a chemometrics-based metabolomic approach. Chemosphere 254, 126812. https://doi.org/10.1016/j.chemosphere.2020.126812.

Ren, L., Xue, X., Zhang, F., Wang, Y., Liu, Y., Li, C., Liang, X., 2007. Studies of iridoid glycosides using liquid chromatography/electrospray ionization tandem mass spectrometry. Rapid Commun. Mass Spectrom. 21, 3039–3050.

Roe, M.K., Junod, N.A., Young, A.R., Beachboard, D.C., Stobart, C.C., 2021. Targeting novel structural and functional features of coronavirus protease nsp5 (3CLpro, Mpro) in the age of COVID-19. J. Gen. Virol. 102 https://doi.org/10.1099/JGV.0.001558.

Ross, I.A., 2003. In: Ross, Ivan, A. (Eds.), Lantana Camara L BT - Medicinal Plants of the World: Volume 1 Chemical Constituents, Traditional and Modern Medicinal Uses. Humana Press, Totowa, NJ, pp. 289–303. https://doi.org/10.1007/978-1-59259-365-1_15.

Saxena, M., Saxena, J., Khare, S., 2012. A brief review on: therapeutical values of Lantana camara plant. Int. J. Phar. Life Sci. 3.

Schoeman, D., Fielding, B.C., 2019. Coronavirus envelope protein: current knowledge. Virol. J. 16 (1 16), 1–22. https://doi.org/10.1186/S12985-019-1182-0, 2019.

Soininen, T.H., Jukarainen, N., Auriola, S.O.K., Julkunen-Tiitto, R., Karjalainen, R., Vepsäläinen, J.J., 2014. Quantitative metabolite profiling of edible onion species by NMR and HPLC–MS. Food Chem. 165, 499–505. https://doi.org/10.1016/j.foodchem.2014.05.132.

Sun, Y.-S., Xu, F., Anb, Q., Chen, C., Yang, Z.-N., Lu, H.-J., Chen, J.-C., Yao, P.-P., Jiang, J.-M., Zhu, H.-P., 2020. A SARS-CoV-2 variant with the 12-bp deletion at E gene. Emerg. Microb. Infect. 9, 2361–2367.

Tiwari, V., 2021. Denovo designing, retro-combinatorial synthesis, and molecular dynamics analysis identify novel antiviral VTRM1.1 against RNA-dependent RNA polymerase of SARS CoV2 virus. Int. J. Biol. Macromol. 171, 358–365. https://doi.org/10.1016/j.ijbiomac.2020.12.223.

Tohmé, M.J., Giménez, M.C., Peralta, A., Colombo, M.I., Delgui, L.R., 2019. Ursolic acid: a novel antiviral compound inhibiting rotavirus infection in vitro. Int. J. Antimicrob. Agents 54, 601–609. https://doi.org/10.1016/j.ijantimicag.2019.07.015.

Vardhan, S., Sahoo, S.K., 2020a. In silico ADMET and molecular docking study on searching potential inhibitors from limonoids and triterpenoids for COVID-19. Comput. Biol. Med. 124, 103936. https://doi.org/10.1016/j.compbiomed.2020.103936.

Vardhan, S., Sahoo, S.K., 2020b. Searching Inhibitors for Three Important Proteins of COVID-19 through Molecular Docking Studies, vol. 148, pp. 148–162.

Vinatoru, M., Toma, M., Radu, O., Filip, P.I., Lazurca, D., Mason, T.J., 1997. The use of ultrasound for the extraction of bioactive principles from plant materials. Ultrason. Sonochem. 4, 135–139.

Wang, Z., Xie, D., Gan, X., Zeng, S., Zhang, A., Yin, L., Song, B., Jin, L., Hu, D., 2017. Synthesis, antiviral activity, and molecular docking study of trans-ferulic acid derivatives containing acylhydrazone moiety. Bioorg. Med. Chem. Lett 27, 4096–4100. https://doi.org/10.1016/j.bmcl.2017.07.038.

Worley, B., Powers, R., 2013. Multivariate analysis in metabolomics. Current Metabolomics 1, 92–107. https://doi.org/10.2174/2213235X11301010092.

Wu, C., Liu, Y., Yang, Y., Zhang, P., Zhong, W., Wang, Y., Wang, Q., Xu, Y., Li, M., Li, X., Zheng, M., Chen, L., Li, H., 2020. Analysis of therapeutic targets for SARS-CoV-2 and discovery of potential drugs by computational methods. Acta Pharm. Sin. B 10, 766–788. https://doi.org/10.1016/J.APSB.2020.02.008.

Xiong, X., Wang, P., Su, K., Cho, W.C., Xing, Y., 2020. Chinese herbal medicine for coronavirus disease 2019: a systematic review and meta-analysis. Pharmacol. Res. 160, 105056. https://doi.org/10.1016/j.phrs.2020.105056.

Xue, Z., Yang, B., 2016. Phenylethanoid glycosides: research advances in their phytochemistry, pharmacological activity and pharmacokinetics. Molecules 21, 1–25. https://doi.org/10.3390/molecules21080991.

Zhao, J., Guo, S., Yi, D., Li, Q., Ma, L., Zhang, Y., Wang, J., Li, X., Guo, F., Lin, R., 2021. A cell-based assay to discover inhibitors of SARS-CoV-2 RNA dependent RNA polymerase. Antivir. Res. 190, 105078.

Zhao, X., Zhang, S., Liu, D., Yang, M., Wei, J., 2020. Analysis of flavonoids in dalbergia odorifera by ultra-performance liquid chromatography with tandem mass spectrometry. Molecules 25, 1–16.